Geochemistry xxx (xxxx) xxx

Contents lists available at ScienceDirect

Geochemistry

journal homepage: www.elsevier.com/locate/chemer

Melt inclusions in spinel from a composite mantle xenolith

Ioannis Baziotis [a,*], Myrto Simopoulou [a], Constantinos Mavrogonatos [b], Stephan Klemme [c], Jasper Berndt [c], Paul D. Asimow [d]

[a] Department of Natural Resources Management and Agricultural Engineering, Agricultural University of Athens, Iera Odos 75, 11855 Athens, Greece
[b] Faculty of Geology and Geoenvironment, National and Kapodistrian University of Athens, Panepistimiopolis, 15784 Athens, Greece
[c] Institut für Mineralogie, Westfälische Wilhelms-Universität Münster, Corrensstraße 24, 48149 Münster, Germany
[d] Division of Geological and Planetary Sciences, California Institute of Technology, Pasadena, CA 91125, USA

ARTICLE INFO

Handling Editor: Jacek Puziewicz

Keywords:
Melt inclusion
Spinel host
Mantle xenolith
Cima Volcanic Field
Trapping and freezing
Amphibole melting
Lithospheric extension

ABSTRACT

Composite mantle xenoliths from the Cima Volcanic Field (CA, USA) contain a variety of melt (now glassy) inclusions hosted within mantle phases. The compositions and textures of these melt inclusions have the potential to constrain their trapping processes, melt sources, and the rates of ascent of their parent xenoliths. Here we focus on unusual spinel-hosted melt inclusions from one composite xenolith, reporting glass and daughter mineral compositions and textures and attempting to reconstruct inclusion bulk compositions. The xenolith contains spinel-hosted melt inclusions in its harzburgite, olivine-websterite and lherzolite layers; there are none in its orthopyroxenite layer.

The glass compositions and reconstructed bulk compositions of the partly-crystallized inclusions correspond to alkaline intermediate melts, mostly trachyandesites. Such melts are most likely to be generated and trapped by vapor-undersaturated phlogopite or amphibole dehydration melting to an assemblage of liquid + spinel + olivine ± pyroxenes. We modeled the near-liquidus phase relations of the inclusion bulk compositions and noted the closest approach of each inclusion to simultaneous saturation with spinel and either phlogopite or amphibole, resulting in estimated trapping pressures of ~0.5–1.5 GPa and temperatures of ~1000–1100 °C. The large size of the hosting spinel grains suggests a slow process associated with these breakdown reactions, probably thinning of the lithosphere and steepening of the geotherm during regional extension.

A linear correlation between the vesicle area and inclusion area (as proxies for volume) suggests an in-situ exsolution process from melts of relatively uniform volatile initial contents, consistent with trapping of vapor-undersaturated melts that later exsolve vapor during cooling and daughter crystal growth. A negative correlation between the glass content in melt inclusions and the size of the inclusion itself suggests a control on the degree of crystallinity with the size. There appears to be a two-stage cooling history captured by the inclusions, forming first prismatic daughter crystals and large round vesicles at the wall of the inclusion, followed by quenching to form a mat of fine crystallites and small vesicles in most inclusions. We connect the final quench to rapid ascent of the xenolith in its host melt, which also triggered partial breakdown of remaining amphibole to fine glassy symplectites.

1. Introduction

The heterogeneity of the Earth's mantle has been extensively studied by a variety of methods, including deep-probing geophysics, variations in the chemical and isotopic compositions of magmas formed by mantle melting, petrographic and geochemical investigations of mantle-derived xenolith specimens of varying lithology brought to the surface by eruptions, and similar studies of mantle outcrops tectonically exposed in massifs (e.g., Begg et al., 2009; Deines, 2002; Menzies et al., 1983; Patkó et al., 2021; Stracke, 2012; Van Keken et al., 2002). In the current study we focus on a layered mantle xenolith, which combines to some extent the advantages of outcrop and conventional xenolith studies by providing a rapidly erupted fresh sample of multiple lithologies with their original contact relations. The contrasting mineral assemblages that define the layering in this composite xenolith (and in other such xenoliths; e.g., Irving, 1980; Patkó et al., 2022) have the potential to

* Corresponding author.
E-mail address: ibaziotis@aua.gr (I. Baziotis).

https://doi.org/10.1016/j.chemer.2024.126118
Received 14 November 2023; Received in revised form 8 April 2024; Accepted 9 April 2024
Available online 15 April 2024

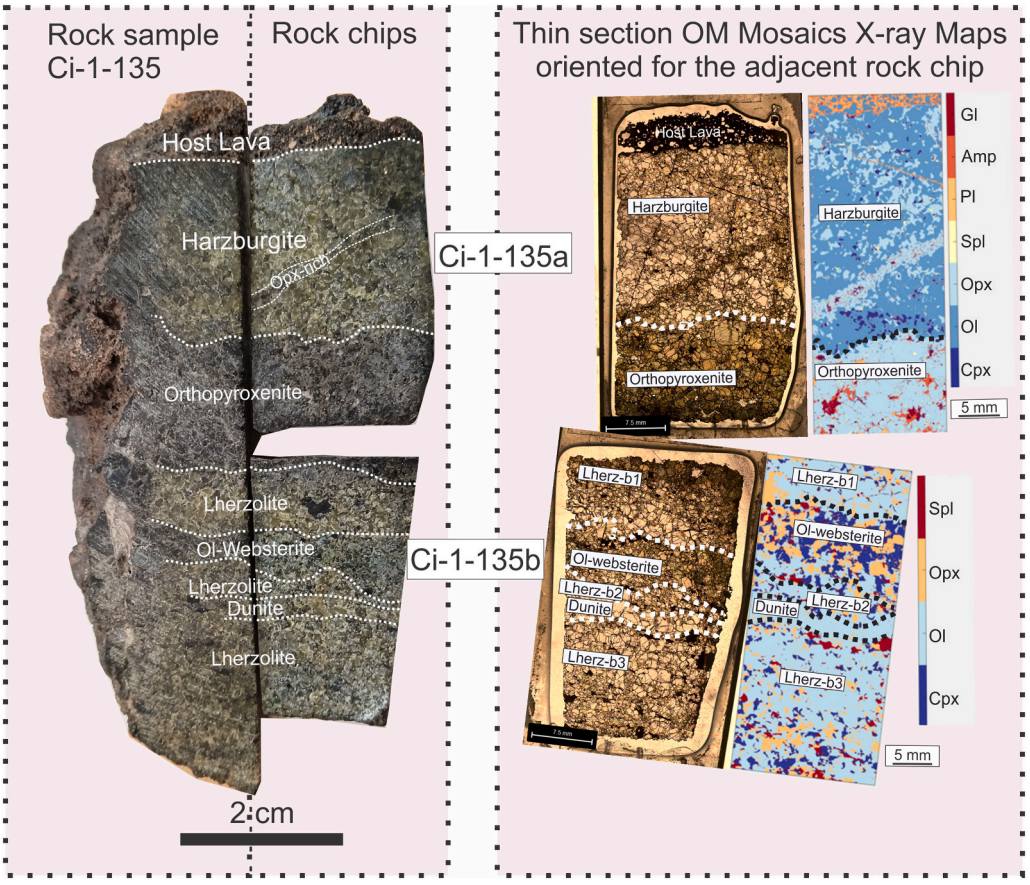

Fig. 1. Photograph of sawn surface of hand-specimen of sample Ci-1-135. The outlines of some lithologically distinct layers are indicated with white dotted lines. Finer-scale layering is also present but not visible at hand-specimen scale; see Figs. S3-S6. Additionally, the distinction of the three lherzolite layers in section Ci-1-135b follows the scheme: "lherz-b1" for the upper lherzolite, "lherz-b2" for the middle lherzolite, and "lherz-b3" for the lower lherzolite.

provide information related to their sources and the petrogenetic processes they have experienced (e.g., partial melting, mantle metasomatism, and crustal contamination). Our particular focus here is on the information recorded by melt inclusions that occur within spinel grains in this xenolith and their relationship (or lack thereof) to the host melt that transported the xenolith to the surface.

Although glassy melt inclusions and embayments have been widely studied in phenocrysts in magmas (e.g., Yaxley et al., 1997; Coltorti et al., 2000; Esposito et al., 2014; Lloyd et al., 2014), they have received less attention in xenoliths. Nevertheless, glasses in mantle xenoliths have been used to provide information on primitive melt compositions, conditions of storage and migration in the mantle, and rates of ascent (e.g., Klügel, 1998; Golovin and Sharygin, 2007). Targets of such xenolith studies include interstitial glasses (e.g., Schiano et al., 2000; Zinngrebe and Foley, 1995), olivine-hosted melt inclusions (e.g., Jannot et al., 2005; Zajacz et al., 2007; Xu et al., 2023), and spinel-hosted melt inclusions (e.g., Ionov et al., 2011; Bénard et al., 2018; Arai et al., 2022). Although studies of spinel-hosted mineral inclusions are not common, they have shown promise for providing information that can be distinct from and therefore complementary to results from the more commonly studied olivine-hosted inclusions. For example, spinel-hosted inclusions may undergo less post-entrapment modification than olivine-hosted inclusions; this idea has been advanced for spinel phenocrysts in mid-ocean ridge picrites (Kamenetsky, 1996) and for cumulus spinel in layered intrusions (Spandler et al., 2000). Spinel-hosted inclusions may also capture the effects of boundary-layer phenomena at crystal-melt interfaces better than olivine-hosted inclusions; this has been argued in the case of phenocrysts in basanite (Longpré et al., 2020).

In this study, we report macro- and micro-scale mineralogical and petrological analyses on constituent minerals and glasses occurring within the different lithologic layers in a composite mantle xenolith from the H. G. Wilshire collection of xenoliths from the Cima Volcanic Field (CVF, California, USA). The composite xenolith contains spinel-hosted glassy inclusions corresponding to former melt inclusions as well as glassy patches surrounding partly decomposed amphibole. We used optical microscopy and electron probe microanalysis (EPMA) in point-analysis and X-ray mapping modes to characterize the glasses, minerals, and vesicles in the various layers of the xenolith. This paper focuses on the mechanisms that formed the trapped melt and on subsequent trapping and freezing processes. A likely mechanism for formation of the melts is breakdown of hydrous phases like amphibole (incongruent melting) and thus we compare our data from inclusions and glassy patches around amphibole to other natural samples and experimental runs that feature amphibole breakdown melting. A subset of the inclusions have exotic K-rich compositions that are more likely to represent phlogopite decomposition melting and may sample a distinctive metasomatic event in the pre-eruptive history of the continental lithosphere of the Mojave region.

2. Geological setting and sample description

The Cima Volcanic Field (CVF) is located in the Mojave Desert, southeastern California, USA (e.g., Wilshire et al., 1991; Luffi et al., 2009) (Fig. S1). The CVF records two major periods of volcanic activity: from ~7.5 to ~3 Ma and subsequently from 1 Ma to the Holocene (Turrin et al., 1985; Nealey and Sheridan, 1989; Wells et al., 1991). Volcanism in the region has been ascribed to crustal extension of the Basin and Range since ~12 Ma (Davis et al., 1993), which has driven

Table 1
Mineral modal content of the whole sections, and separate lithological layers in sample Ci-1-135.

	ol	opx	cpx	spl	amph	pl	gl	Designation
Ci-1-135a								
Whole section	48.6	42.6	2.9	1.1	2.6	0.5	1.8	Harzburgite
Lower layer	2.5	81.9	1.6	1.6	6.7	1.1	4.6	orthopyroxenite
Upper layer	67.1	27.0	3.3	0.8	0.9	0.2	0.7	harzburgite
Ci-1-135b								
Whole section	60.8	19.0	16.1	4.1	–	–	–	Lherzolite
Central pyroxene-rich layer	25.2	36.9	33.7	4.2	–	–	–	Olivine websterite
Lherz-b1	75.5	16.7	6.7	1.1	–	–	–	Lherzolite
Lherz-b2	71.6	13.2	12.8	2.6	–	–	–	Lherzolite
Lherz-b3	76.5	10.2	9.0	4.3	–	–	–	Lherzolite
Dunite	95.2	3.8	0.5	0.5	–	–	–	Dunite

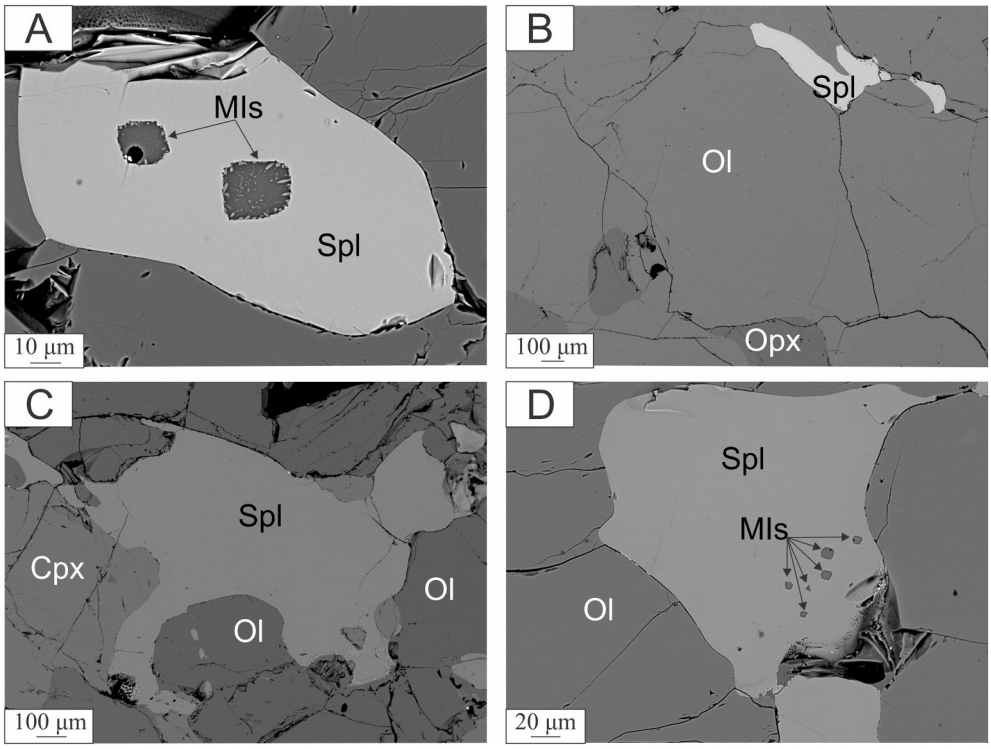

Fig. 2. Anhedral to euhedral interstitial spinel grains are widespread along grain boundaries and at contacts between the layers from the sections Ci-1-135a (A,B) and Ci-1-135b (C,D). The spinel grains in (A,B) are from the harzburgite, in (C) from the ol-websterite and in (D) from the lherzolite layer (lherz-b1).

both felsic volcanism associated with crustal unroofing in Cordilleran metamorphic core complexes and mafic volcanism associated with mantle decompression (Wells and Hoisch, 2008). The CVF is dominated by alkaline magmas: most eruptions range from trachybasalt (hawaiite to potassic trachybasalts including both nepheline- and hypersthene-normative samples; Le Maitre, 1989) to basaltic trachyandesite (hypersthene-normative mugearite; Wilshire et al., 1988, 1991; Mukasa and Wilshire, 1997; Farmer et al., 1995).

Mantle xenoliths occur in CVF magmas at several localities and have been well studied and characterized in terms of their fabric, age, mineralogy, geochemistry, petrology, density, and thermal history in order to evaluate the melting conditions, magmatic processes, thermal structure, and landscape evolution of the Basin and Range province (Wilshire et al., 1991; Farmer et al., 1995; Mukasa and Wilshire, 1997; Luffi et al., 2009; Plank and Forsyth, 2016; Bernard and Behr, 2017; Baziotis et al., 2017, 2019; Valentine et al., 2021; Brehm and Lange, 2023). The CVF xenolith suite has been divided into a "Cr-diopside" group (peridotite, websterite, phlogopite ± pargasite clinopyroxenite), a "low-Cr green-pyroxene" group (Mg-rich websterite, two pyroxene gabbro, microgabbro), and an "Al-augite group" (Fe-rich websterite, clinopyroxenite, gabbro and microgabbro) (e.g., Wilshire et al., 1985, 1991; for the location of the three xenolith groups see Figs. 3, 4, and 7 in Wilshire et al., 1985). A fourth group includes composite xenoliths sampling two or more of the previous lithologies or containing hornblend ± plagioclase ± phlogopite veins up to 15 mm wide (Irving, 1980; Farmer et al., 1995; Wilshire et al., 1991; Wilshire and McGuire, 1996).

We describe here in detail one such composite xenolith: sample *Ci-1-135* from the Howard Wilshire collection archived at the Smithsonian Institution (NMNH 118016-148). It is amphibole-bearing, with layering defined by differences in modal mineralogy at hand-sample and thin-section scale. Recognized layers include dunite, olivine-websterite, harzburgite, and coarse-grained lherzolite (Figs. 1, S2). In harzburgite, olivine-websterite and lherzolite layers, spinel-hosted glassy inclusions display a variety of textures and a range in degree of crystallization, from pure glass to fully crystalline (Fig. 1). We selected this xenolith for study of preserved boundaries between mantle lithologies, as reported in Baziotis et al. (2017). The overall mineral assemblage includes olivine, clinopyroxene, orthopyroxene, spinel, plagioclase, and amphibole, although the proportions vary from layer to layer (for details of the modal abundances of the lithologic layers of the studied sections see

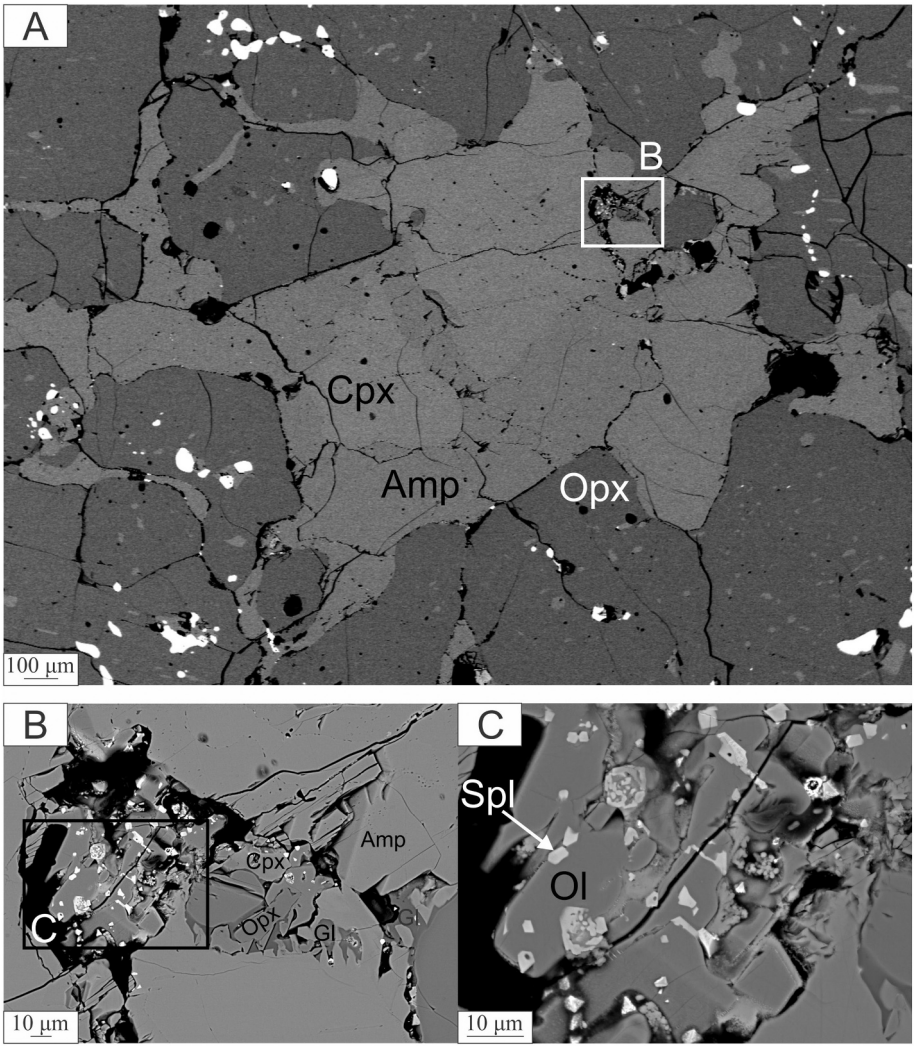

Fig. 3. (A) Amphibole located within the orthopyroxenite layer (section Ci-1-135a). The location of a pocket enlarged in panel B is indicated. (B) The pocket contains amphibole breakdown features suggested by the presence of newly formed spinel+olivine+clinopyroxene+glass. The area further enlarged in panel C is indicated. (C) Secondary spinel coexisting with olivine in the amphibole decomposition area. Abbreviation: Gl: glass.

Table 1; mineral abbreviations in tables, figures, and text are from Whitney and Evans, 2010). Anhedral to euhedral interstitial spinel grains are widespread along grain boundaries and at contacts between the layers (Figs. 1, 2, S3-S6). In several places, amphibole is rimmed by dark brown aggregates of glass and fine secondary crystals, suggesting partial melting, presumably upon rapid decompression (e.g., Baziotis et al., 2013).

3. Methods

3.1. Optical microscopy and back-scattered electron microscopy

We studied two polished thin sections from sample *Ci-1-135*. Section *Ci-1-135a* is cut across the boundary of the inclusion and includes some of the host basalt. Section *Ci-1-135b* is an interior cut, several cm from the nearest host basalt in any direction (Fig. 1). Petrographic descriptions of these two sections were based on optical microscopy and on back-scattered electron (BSE) images; the latter were acquired with a field-emission (FE) electron probe micro-analyzer (EPMA) JEOL JXA8530F at the Institut für Mineralogie, University of Münster (Germany).

3.2. Electron probe micro-analyzer

Major element compositions of minerals were also determined using the JEOL JXA8530F (at the Institut für Mineralogie, University of Münster, Germany). It is equipped with five wavelength-dispersive spectrometers (WDS) and one energy-dispersive spectrometer. All analyses were performed with an accelerating voltage of 15 kV. For minerals, we chose a 15 nA focused beam current and 20 s on-peak counting time and 10 s for each background. For glass analyses, we applied a slightly defocused (5 μm diameter) beam and 10 s counting time. We also collected broad-beam (20–30 μm diameter) analyses to average over glass and daughter crystals and estimate bulk composition of inclusions. Natural mineral standards used were albite (Na, Si, Al), wollastonite (Ca), Mongolia olivine (Mg), almandine (Fe), spessartine (Mn), orthoclase (K), rutile (Ti), chromite (Cr), Ni-oxide (Ni) and Durango apatite (P). Additionally, we applied a higher-precision analytical protocol to quantify minor elements in olivine from each layer: 15 kV accelerating voltage; 120 nA focused beam current; 60 s counting time on peak and 30 s on each background for Na, Al, Ti, Mn, Cr, Co, Ni, P, and Ca; 10 s on peak and 5 s on each background for Si, Mg, and Fe. For this protocol we did not use albite as a standard, choosing instead beam stable standards Jadeite (Na), San Carlos Olivine (Mg), kyanite (Al), Mongolia Olivine (Si), Rutile (Ti), Rhodonite (Mn), Fayalite

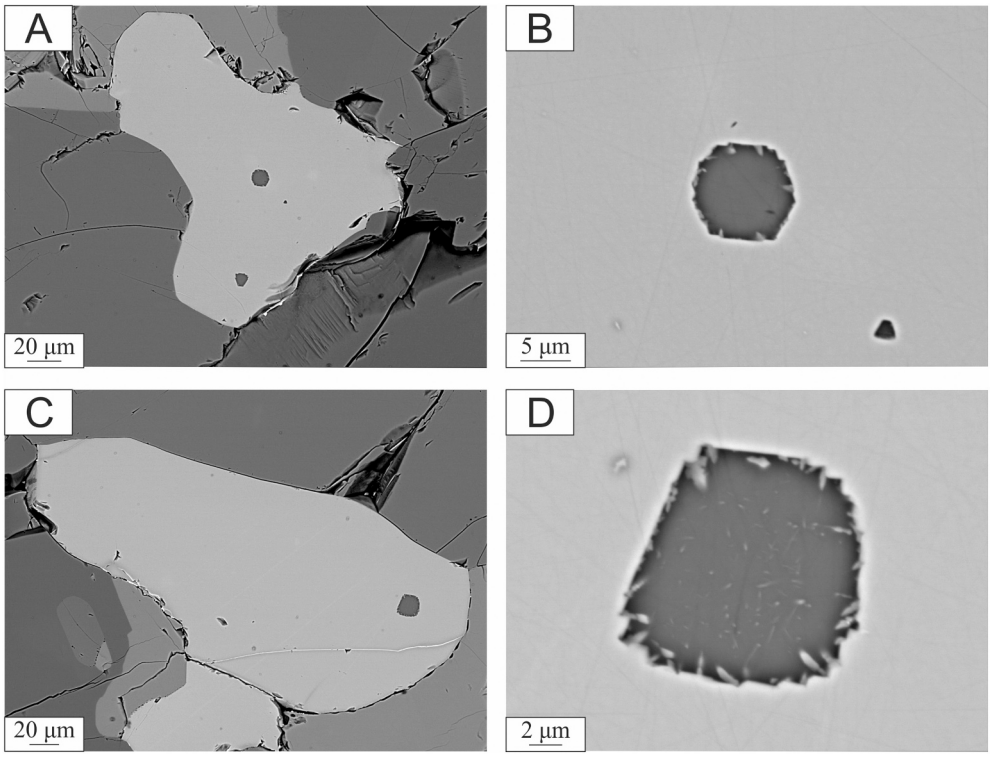

Fig. 4. Backscattered electron (BSE) images of melt inclusions in spinel from section Ci-1-135a. (A) Spinel hosting two glassy inclusions (B) Enlarged image of the glassy inclusion given in (A). (C,D) Spinel hosting a partly crystallized inclusion. All spinels are from the harzburgite layer.

(Fe), Cr_2O_3 (Cr), Co (Co), NiO (Ni), Apatite (P), and diopside (Ca).

3.3. X-ray maps and their manipulation

We acquired quantitative X-ray map mosaics of each complete section. These maps were acquired at 15 kV, 50 nA, focused beam, stage scan in 25 μm steps, and making two mapping passes to measure ten elements (Si, Ti, Al, Cr, Fe, Mg, Ca, Na, K, P). In addition, after completing point analyses of phases within the inclusion, we obtained a detailed high-resolution X-ray map of a partially-crystallized spinel-hosted inclusion in *Ci-1-135b* using the same protocol with stage scan in 0.1 μm steps. The quantitative maps were processed off-line for modal analysis and bulk composition estimation using the free Software XmapTools ver. 4.1 (Lanari et al., 2014, 2019, 2023). The bulk composition reconstruction from X-ray maps was applied as (1) a check on the broad-beam method of estimating bulk composition of the mapped melt inclusion, (2) as a means of estimating the pre-quench liquid composition of the inclusions, and (3) as a means of estimating the bulk composition of the host lava. The process we followed can be found in a detailed tutorial at https://xmaptools.ch.

4. Results

4.1. Petrography

Phase compositions of the primary minerals are presented in the supplementary section (Tables S1-S5; see also supplementary Text S1). The nomenclature based on the modal abundance of olivine, orthopyroxene, and clinopyroxene in each layer is given in Fig. S2.

4.1.1. Ci-1-135a

Section *Ci-1-135a* samples two main layers of the xenolith, the harzburgite and orthopyroxenite domains (Figs. S3, S4). The texture of the harzburgite is coarse-grained with grain sizes in the range of 500–1500 μm, and that of the orthopyroxenite is porphyroclastic (Mercier and Nicolas, 1975). The orthopyroxenite layer is amphibole- and plagioclase-bearing (Figs. 1, S3; Table 1). The amphibole is in contact with both orthopyroxene and clinopyroxene and is partly decomposed to Cr-spinel+olivine+glass (Fig. 3). One distinct orthopyroxene-rich vein penetrates the harzburgite layer at an orientation discordant to the general layering of the xenolith (Figs. 1, S3). There is a clinopyroxene-rich band in the harzburgite, subparallel to the boundary with orthopyroxenite (right panel of Fig. S3). There are also a few discrete cracks filled with host basalt material, <1 mm wide but penetrating several cm into the xenolith (Fig. 1).

4.1.2. Ci-1-135b

Section *Ci-1-135b* is cut from the interior of the xenolith (3.65 cm away from the melt-xenolith boundary) and lacks host basalt-filled cracks. This section crosses an olivine(ol)-websterite layer separating two thick low-clinopyroxene lherzolite layers (lherz-b1; lherz-b3) (Figs. S5, S6; Table 1). Also, there is a continuous olivine band across the section that could be distinguished as a dunite layer (Figs. 1, S5). Another thin lherzolite layer occurs between the ol-websterite and the dunite layer, named as lherz-b2 in Fig. 1. The spinels occur within all the layers, but those in the ol-websterite are located mainly at the contacts with the lherzolite layers (Figs. S5, S6). In layers lherz-b2 and lherz-b3, some spinel grains are larger than 1 mm in diameter.

4.1.3. Melt inclusions

We have observed 35 melt inclusions (MIs) exposed in the two sections of sample *Ci-1-135*, all enclosed in spinel. Spinel being optically opaque, we were unable to observe or count unexposed inclusions below the polished surfaces. These inclusions (number of MIs is given in parentheses) are located in the harzburgite (5) layer of *Ci-1-135a* and in the ol-websterite (14), lherz-b2 (3), and lherz-b3 (13) layers of *Ci-1-135b*. We were unable to locate any melt inclusions in any host phase in the orthopyroxenite layer. The MIs in harzburgite are located within the interior of the layer; there are two spinel grains in harzburgite that host two inclusions each and an additional spinel grain hosts one inclusion. In

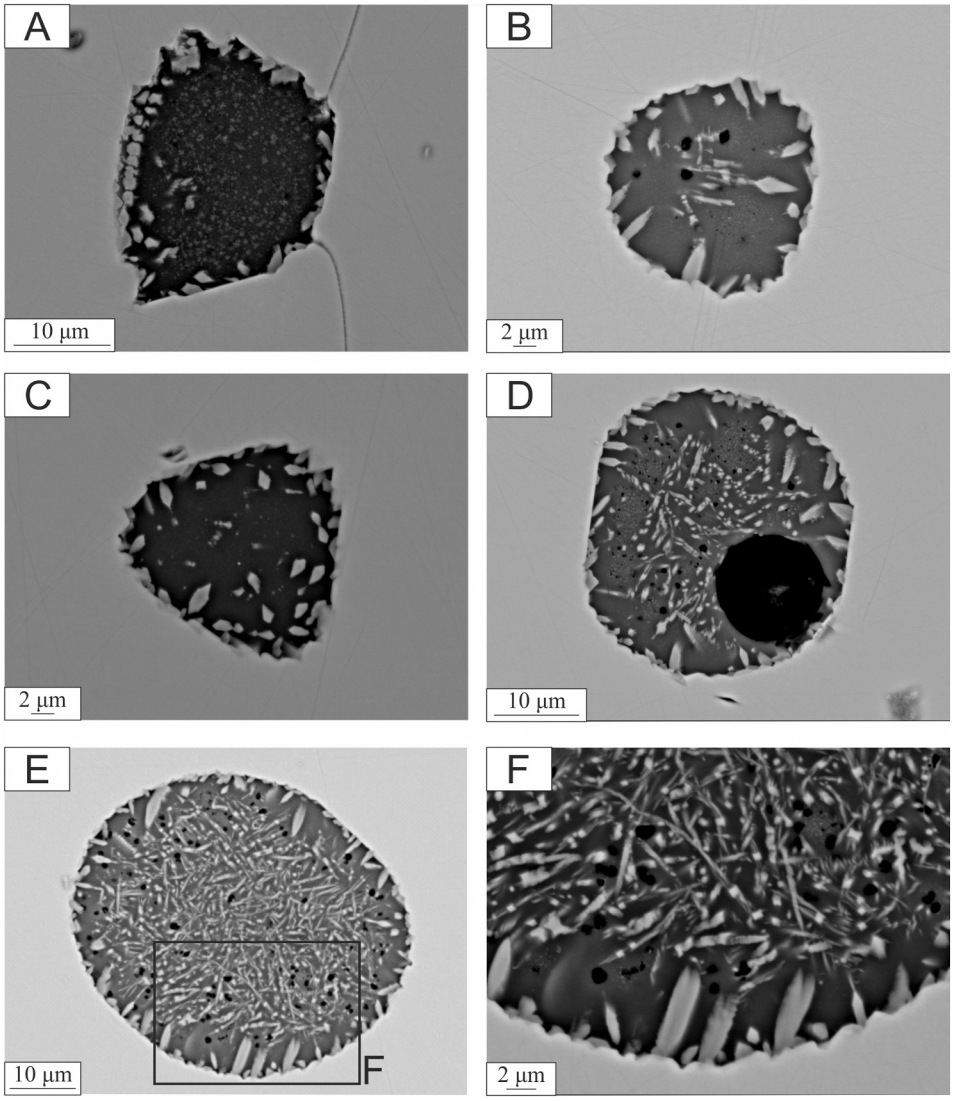

Fig. 5. BSE images of melt inclusions in spinel from section Ci-1-135b. (A) An inclusion containing glass, and boundary clinopyroxene crystals. (B) Inclusion with glass, no visible microlites, minor vesicles, and elongated clinopyroxene crystals. (C) Similar to (B) with rhombohedral clinopyroxene crystals. (D) Inclusion with both quench crystals and prismatic boundary crystals as well as two sizes of vesicle; large vesicle touches the host spinel. (E) Heavily quench-modified inclusion with numerous small crystals and vesicles, see Fig. 8. (F) Enlarged view of the margin of inclusion from (E). The spinel grains are from the lherzolite layer (lherz-b3).

contrast, the MIs in ol-websterite are all found in two large spinel grains close to the contact with lherz-b1, hosting six and eight MIs, respectively. Similarly, the MIs in the lherz-b2 and lherz-b3 layers are found exclusively close to the boundary with the adjacent dunite layer. All three MIs in lherz-b2 are found in one spinel grain, whereas the 13 MIs in the lherz-b3 layer are distributed across 12 spinel grains (only one of these grains has two MIs). We measured the dimensions (short and long axis) for 24 of these MIs (Table S6). Twenty (83 %) of the measured MIs are nearly equant, with aspect ratios in the range of 1.06–1.3, whereas four are elongated, with aspect ratios from 1.43 to 2.02.

Among the 24 MIs we studied in detail, all but one are at least partly crystallized (Table S6). The five melt inclusions in the harzburgite layer of section *Ci-1-135a* are the least crystallized (Fig. 4). One of these is entirely glassy in its interior (at least at the resolution of field-emission BSE imaging); it has a negative crystal shape, hexagonal in cross section, and has only a few elongated pyroxene crystals radiating from the inclusion wall (Fig. 4B). Another inclusion in the same spinel grain–located close to the lower edge of the spinel–is nearly crystal-free in its interior (97.9 % glass) and has one planar face and three rounded faces (Fig. 4A). Another spinel from the harzburgite layer contains one inclusion with a few crystallites that are too small to analyze (i.e., ≤0.5 μm) (Fig. 4C, D). The two inclusions in another spinel grain in harzburgite (Fig. 2A) have a glass content in the range 86–94 %. One contains a large vesicle breached by the polished surface. The sparse crystals in the MIs in harzburgite layer are aluminous clinopyroxene (see Section 4.2.1), 0.3 to 4.6 μm in maximum dimension with mostly elongated shapes (aspect ratios 1.04–5.36).

The MIs in the ol-websterite and lherzolite layers of section *Ci-1-135b* display a variety of textures (Figs. 5, 6), all more crystalline than the MIs in harzburgite. Many MIs contain vesicles, which fall into two classes. “Group I" vesicles are small (~1 μm diameter), subrounded in shape, and occur in clusters among meshes of fine elongated or dendritic pyroxene and spinel crystals (e.g., Fig. 5B, D-F, 6E). Group I vesicles are found in 11 (~46 %) of the observed MIs. “Group II” vesicles are large (~10 μm in diameter) spherical vesicles (Figs. 5D, B, 6E), never more than one per MI, which are always seen in direct contact with the host spinel. These larger vesicles often have BSE-bright haloes (Fig. 6B); occasionally small group I vesicles have BSE-bright haloes as well. In one case, a daughter sulfide crystal was observed on the inner wall of a group-II vesicle (Fig. 6E). Group II vesicles are found in 14 (58.3 %) of the observed MIs.

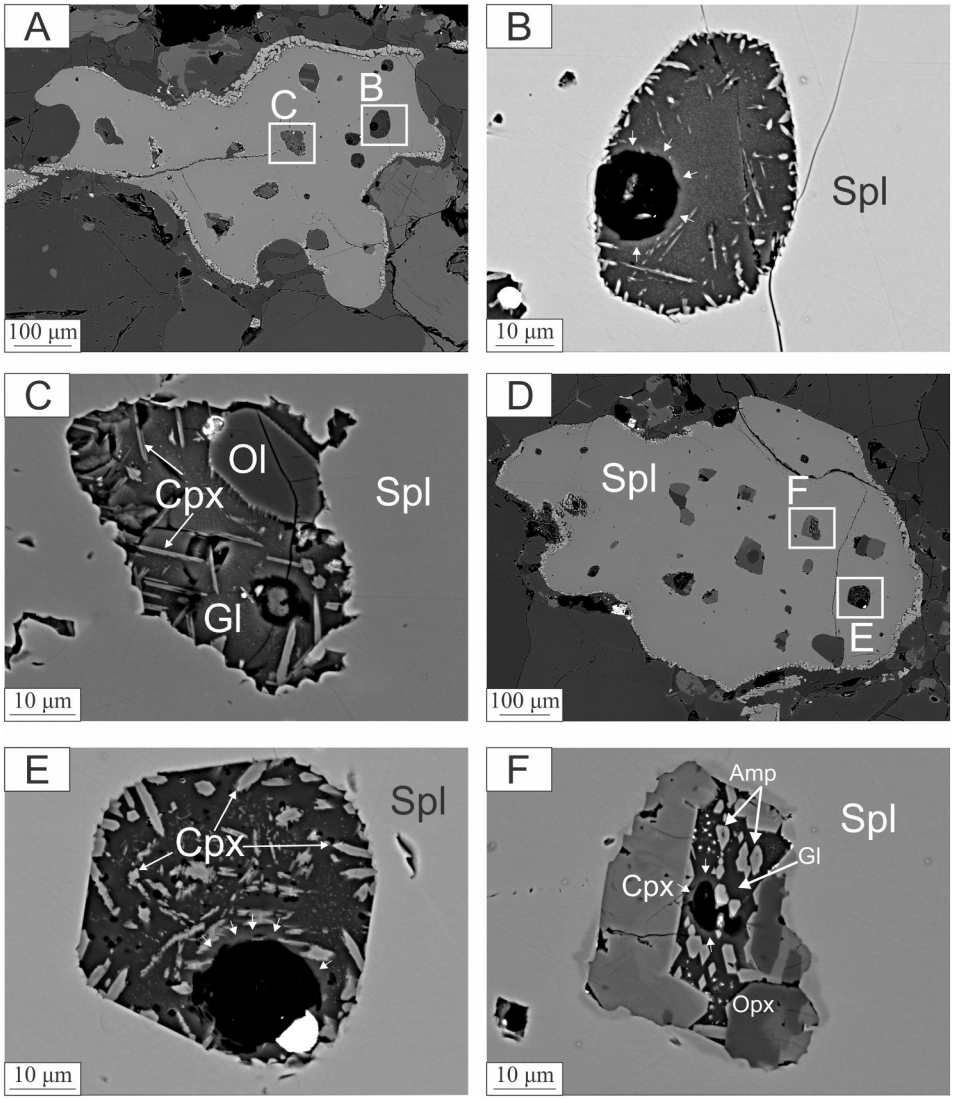

Fig. 6. BSE images of melt inclusions in spinel from section Ci-1-135b. (A) Anhedral spinel hosts numerous inclusions with a variety of textures. (B) Quenched crystals in glass and a large vesicle in contact with host spinel. (C) Complex inclusion with glass, oriented clinopyroxene, and a large euhedral olivine crystal with dimensions 11 × 18 μm. (D) Another anhedral spinel with different textures in its melt inclusions. (E) Quenched and boundary clinopyroxene crystals and two sizes of vesicle; the large vesicle in context with the host spinel contains a daughter sulfide grain. (F) A composite inclusion containing clinopyroxene + orthopyroxene + glass + amphibole. The arrows in panels B, E, F point to the bright halo around the large vesicle. The spinel grains are from the ol-websterite layer.

Both Group I and Group II vesicles are seen in 7 (~29 %) MIs, whereas 7 MIs (also ~29 %) do not have any vesicles exposed at the polished surface (more details on Section 5.3, and supplementary text Section S2).

The MIs in the layers of section *Ci-1-135b* mostly consist of glass plus variable fractions of elongated aluminous pyroxene in two populations separated by size. In the ol-websterite layer, these pyroxene crystals have long axis lengths between 0.3 and 10.6 μm and aspect ratios from 1.04 to 19.0. In the lherz-b2 layer, the pyroxene crystals have long axis lengths from 0.3 to 4.6 μm and aspect ratios from 1.3 to 7.4. The pyroxene crystals in MI from the lherz-b3 layer have long axis lengths from 0.2 to 8.6 μm and aspect ratios from 1.4 to 18.2. The crystals larger than ~2 μm in each case are typically euhedral, more equant, and often attached to the MI boundary. The crystals smaller than ~2 μm are more acicular and uniformly distributed through the volume of the MI.

Two MIs in the ol-websterite layer are different from the others. One inclusion with dimensions 26.9 × 54.3 μm contains a euhedral olivine (11 × 18 μm) in addition to glass and clinopyroxene (Fig. 6C). The clinopyroxene crystals in this inclusion are elongated (aspect ratio ~12.5, short axis lengths 0.2–0.8 μm, long axis 5–12 μm) and display three preferred orientations on the plane of the section. We were unable to obtain reliable quantitative analyses of these clinopyroxene grains. The second anomalous MI, 27.9 × 40.0 μm and irregular in shape, contains clinopyroxene + orthopyroxene + glass + amphibole (Fig. 6F). Approximately 45 % of the melt inclusion area is filled by a single clinopyroxene crystal (12 × 40 μm). There are two orthopyroxene crystals, both euhedral to subhedral and 13 × 14 μm in size. The orthopyroxene crystals host irregular clinopyroxene inclusions up to 2 × 8 μm. Amphibole is present as small euhedral crystals (2.0 × 3.5 μm) embedded in the glass.

We plotted the modal glass fraction (in %) within the MIs against the short and long axis dimensions of each measured inclusion, as a test of whether the size of the MI influences the degree of crystallinity (Fig. 7). There is a broad negative correlation, with larger inclusions (especially measured by long axes) being typically more crystallized. The highly glassy MIs in the harzburgite layer are also the smallest MIs in the population.

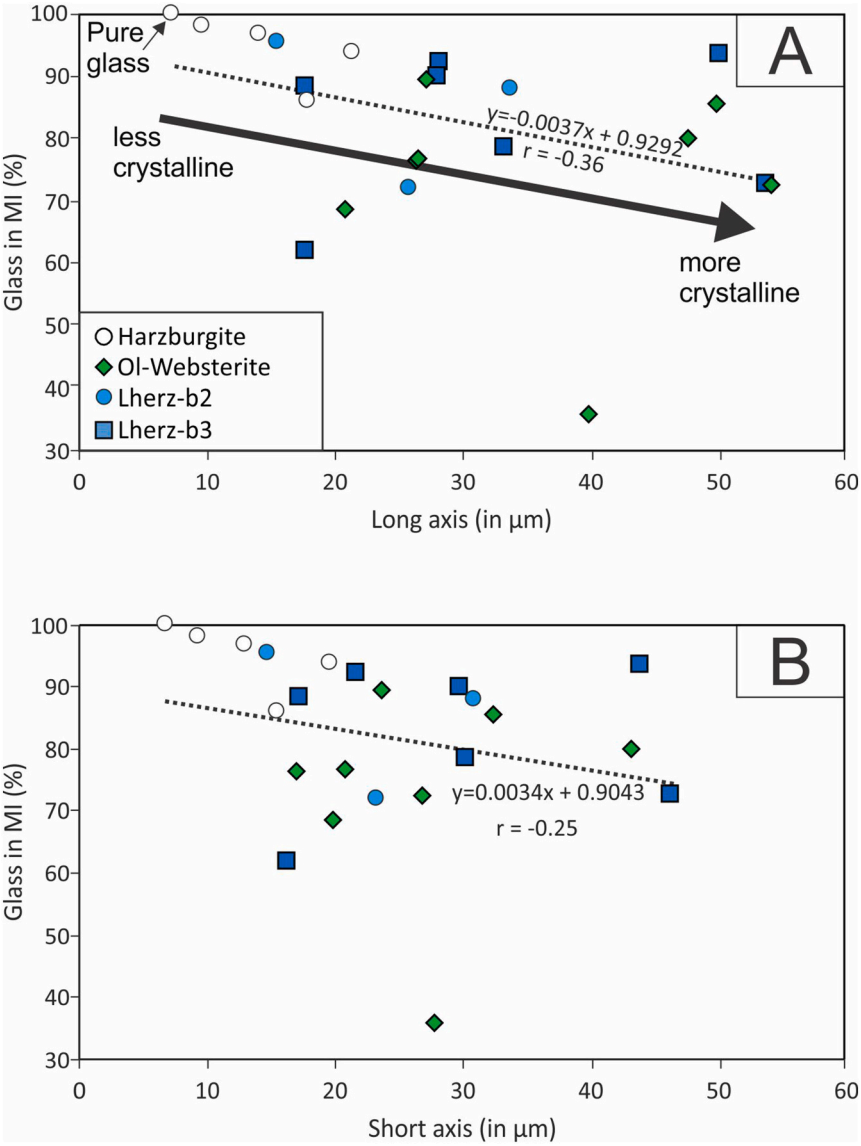

Fig. 7. Modal glass abundance (in %) in MIs plotted vs. (A) long axis and (B) short axis length of each measured inclusion.

4.2. Mineral and glass compositions

The major element compositions of the primary phases within the xenolithic layers are presented in the supplementary text and figures (Figs. S7-S11). The major element compositions of glass inside the melt inclusions are presented in this section and the analytical data are given in Table S7. Wherever possible, we analyzed glass from all distinguishable textural types of melt inclusions in each lithology (*harzburgite*, *ol-websterite*, *lherz-b2*, *lherz-b3*). In particular, the number of analyzed and plotted individual glass analyses are as following: 8 in harzburgite, 17 in ol-websterite, 5 in layer lherz-b2, and 13 in layer lherz-b3. Most secondary crystals in the inclusions were too small to analyze accurately with the microbeam techniques applied. However, we have obtained 11 single spot analyses from the elongated clinopyroxene crystals inside the melt inclusion shown in Fig. 5E (see also Figs. 5F, 8, S12). The large olivine in an inclusion in ol-websterite noted above is also large enough in two dimensions to yield an accurate analysis free from beam overlap and secondary fluorescence artifacts. Later we will also present broad-beam analyses that average over glasses and small secondary phases to estimate bulk inclusion compositions.

4.2.1. Inclusion glasses in harzburgite layer (section Ci-1-135a)

Glasses in harzburgite display a range of compositions, with SiO_2 53.1–59.5 wt%, K_2O 1.90–5.60 wt%, Na_2O 2.25–7.62 wt%, CaO 1.31–2.66 wt%, and P_2O_5 0.19–0.55 wt% (Figs. 9, 10). The analyses divide into two groups. Two inclusion glasses, found in different host spinels, plot as tephriphonolite on the TAS plot and define a low-SiO_2, low-CaO, high-K_2O, very high Cr_2O_3 group (Fig. 9). The other inclusion glasses are mostly trachyandesite, plus one low-Na_2O analysis that plots in the andesite field. There are no notable correlations among oxide concentrations with this andesite-trachyandesite group. In a FeO^T/MgO vs. SiO_2 diagram, all the glasses from the harzburgite plot in the low-Fe calc-alkaline field (Fig. 10). All the harzburgite-hosted inclusion glasses plot in or just on the edge of the high-K calk-alkaline field on a SiO_2 vs K_2O variation diagram.

4.2.2. Glasses in orthopyroxenite layer – around amphibole (section Ci-1-135a)

Glass occurs in decomposition patches around amphibole in the orthopyroxenite layer (Fig. 3); two spots were large enough to obtain clean analyses with a defocused beam. They display the following compositional range: SiO_2 60.6–64.6 wt%, K_2O 2.44–2.72 wt%, Na_2O 4.39–5.95 wt%, CaO 1.45–2.93 wt%, TiO_2 1.87–2.42, and P_2O_5

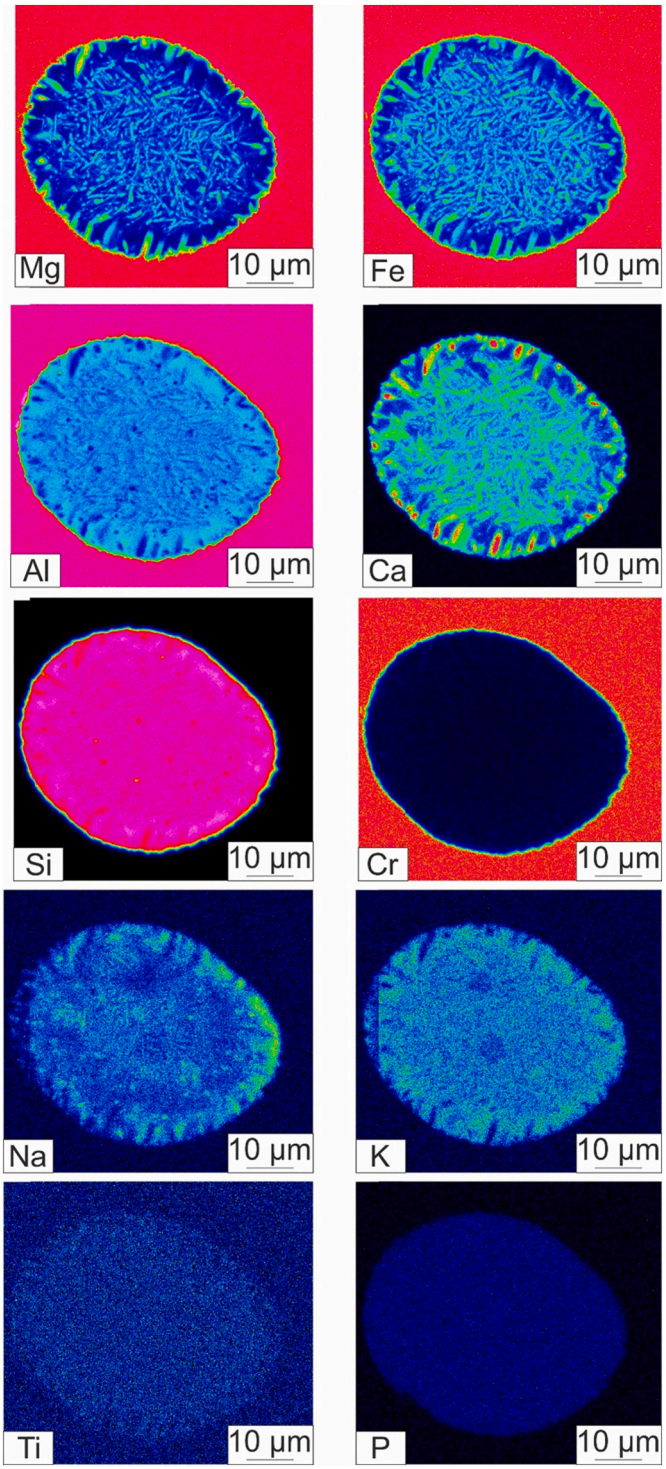

Fig. 8. WDS X-ray maps for selected elements (Mg, Al, Fe, Ca, Si, Cr, Na, K, Ti, P) from a melt inclusion inside a spinel (section Ci-1-135b). Colour scale varies from black (lowest counts), through blue-green-yellow-red-purple to white (highest counts). The spinel grain is from the lherzolite layer (lherz-b3). (For interpretation of the references to colour in this figure legend, the reader is referred to the web version of this article.)

0.53–0.57 wt% (Figs. 9, 10). One spot analysis plots as trachyandesite on the TAS plot, while the other plots as dacite (Fig. 9). Both analyses are marked by low Cr_2O_3 and high TiO_2 for their SiO_2 content (Fig. 10A, C). Furthermore, both analyses plot on a common trend with glass observed around amphibole in another CVF sample (*Ci-1-196*) in the TiO_2 vs. SiO_2 diagram, extending the trend to higher SiO_2 content (Fig. 10A). In a FeO^T/MgO vs. SiO_2 diagram, the low silica analysis plots in the tholeiitic field, while the high-SiO_2 analysis is in the low-Fe calk-alkaline field (Fig. 10F). Both glasses plot within (though close to the lower boundary of) the high-K field on a SiO_2 vs K_2O variation diagram (Fig. 10I).

4.2.3. *Inclusion glasses in ol-websterite and lherzolite layers (section Ci-1-135b)*

Glasses in the MIs in spinel in the ol-websterite and lherzolite layers (Figs. 9, 10) are more diverse than those observed in the harzburgite layer. In ol-websterite, the MIs show the following compositional range: SiO_2 52–64.8 wt%, K_2O 0.43–4.63 wt%, Na_2O 1.95–9.54 wt%, CaO 1.21–9.10 wt%, and P_2O_5 0.34–1.23 wt%. They spread across many fields of the TAS classification diagram, but can be divided into four groups on the basis of the FeO^T/MgO vs. SiO_2 classification diagram: a low-Fe calc-alkaline group, a medium-Fe calk-alkaline group, a medium-Fe tholeiitic group, and a high-Fe tholeiitic group. The three inclusions in the lherz-b2 layer display a more restricted compositional range in most oxides: SiO_2 57.3–59.1 wt%, K_2O 0.59–3.18 wt%, Na_2O 5.24–7.82 wt%, CaO 2.17–4.00 wt%, and P_2O_5 0.32–0.75 wt%. In a FeO^T/MgO vs. SiO_2 diagram, all the glasses from the lherz-b2 layer are classified as low-Fe calc-alkaline. The larger number of inclusion glasses analyzed from the lherz-b3 layer are heterogeneous in oxide composition (SiO_2 55.4–66.3 wt%, K_2O 0.22–2.67 wt%, Na_2O 0.51–8.88 wt%, CaO 2.17–4.34 wt%, and P_2O_5 0.22–0.70 wt%) yet all but one analysis from this layer plot in the low-Fe calc-alkaline field of the FeO^T/MgO vs. SiO_2 diagram; the exception corresponds to a medium-Fe calc-alkaline glass.

4.2.4. *Crystalline phases in Ci-1-135a*

Olivine in the amphibole melt pocket is unzoned (Fig. 3C) and is iron enriched (Fo_{83-84}) compared to the primary olivine of all the other layers ($Fo_{83.7-87.3}$ from the harzburgite layer excluding the values of $Fo_{77.6-73.2}$ when the olivine is close to the contact with the host lava, $Fo_{88.1-88.4}$ from the ol-websterite, $Fo_{87.2-87.8}$ from lherz-b1, $Fo_{86.7-87.0}$ from the lherz-b3 layer). Concentrations of MnO, NiO and Cr_2O_3 are in the range of 0.17–0.18 wt%, 0.25–0.27 wt% and 0.09–0.10 wt%, respectively. These MnO concentrations are in the same range as the primary olivine (0.14–0.49 wt% from the harzburgite layer, and 0.12–0.21 wt% from the ol-websterite and lherzolite layers), whereas the NiO is at the lower end of concentrations noted among primary olivine (0.08–0.40 wt% from the harzburgite layer, and 0.28–0.42 wt% from the ol-websterite and lherzolite layers) analyses. The CaO content is in the range 0.28–0.33 wt %, higher than primary olivine in sample *Ci-1-135*, except where the olivine rim is in contact with the host lava. The P_2O_5 content, 0.11–0.16 wt%, is also higher than in any primary olivine analysis ($P_2O_5 \leq 0.07$ wt %) from any other layer.

4.2.5. *Crystalline secondary phases in Ci-1-135b*

Although we observe daughter crystals including clinopyroxene, amphibole, oxide, and sulfide in inclusions in section *Ci-1-135b*, the only daughter phases we succeeded in analyzing were elongated pyroxene crystals (11 spots; Table S8) in one spinel-hosted MI in lherz-b3 (Fig. 5E, F; lherz-b3 layer) and a large olivine (one spot) in an inclusion in spinel in the ol-websterite layer (Fig. 6C).

The clinopyroxene analyses from the inclusion in lherz-b3 are notably more Fe-rich (Mg# = 0.62–0.75) than any of the primary pyroxene from the xenolith (Mg# = 0.85–0.98) and span a large range in CaO content (7.7–14.1 wt% in inclusion from lherz-b3; 18.0–21.4 wt% in primary pyroxene), projecting along a roughly linear array $Wo_{5-35}En_{40-70}Fs_{23-26}$ (Fig. S5A). The Al_2O_3, Cr_2O_3, Na_2O and TiO_2 content is in the range of 11.9–15.8 wt%, 0.39–0.89 wt%, 0.43–0.87 wt% and 0.37–1.14 wt%, respectively.

The analysis of olivine in an inclusion has Fo content ($Fo_{87.7}$) within the range of olivine from the groundmass ($Fo_{86.7-88.4}$). However, it is enriched in TiO_2 (0.17 wt%), Al_2O_3 (0.28 wt%), CaO (0.31 wt%), and Cr_2O_3 (0.56 wt%), and depleted in NiO (0.30 wt%) compared to primary

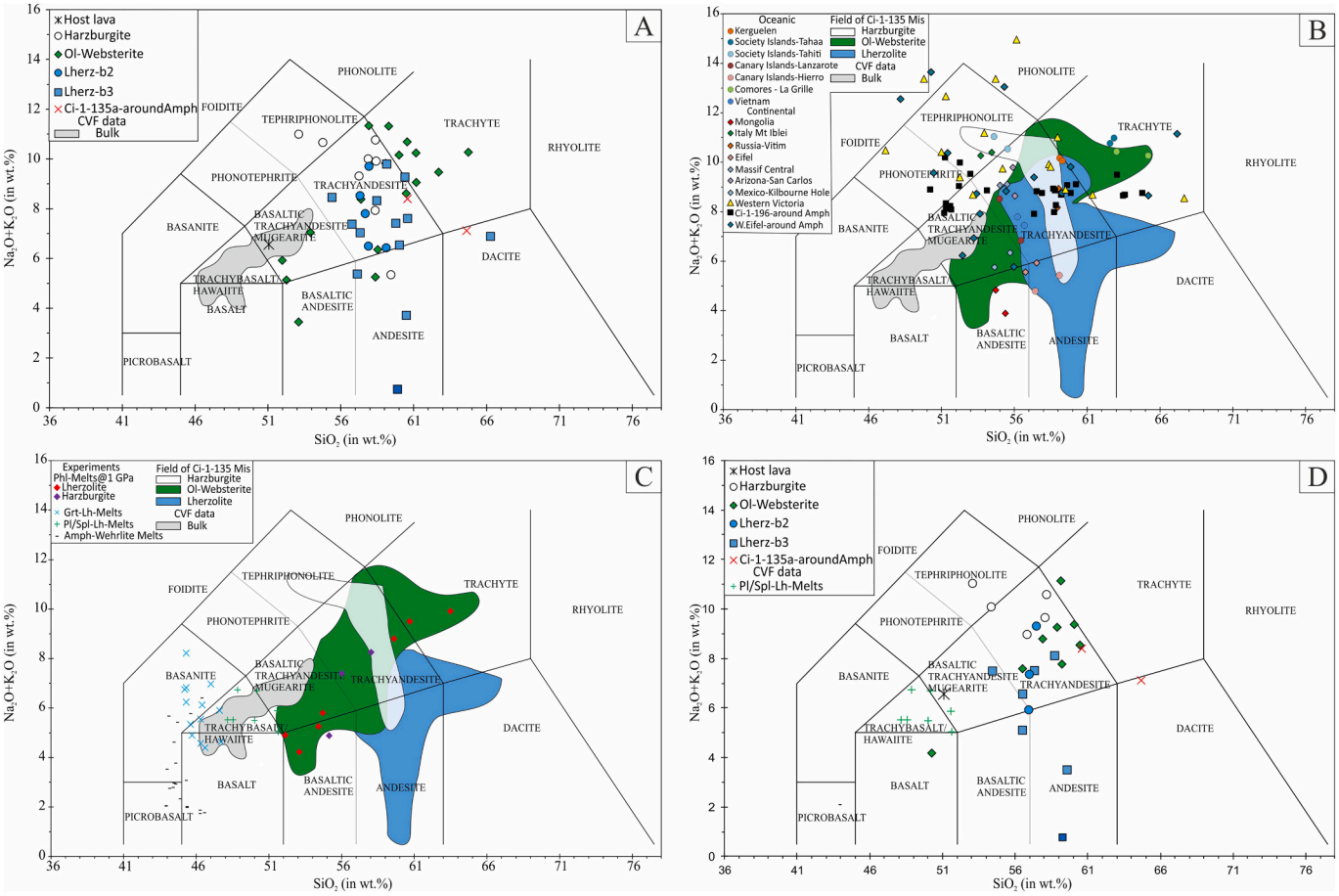

Fig. 9. (A) TAS diagram of glass in xenolith Ci-1-135, found as inclusions in various layers and as patches around amphibole, along with the host lava composition and a field for the diverse lavas of the CVF. The bulk composition of the host lava, estimated from X-ray map reconstruction, is SiO_2: 51.10 TiO_2: 2.35 Al_2O_3: 19.2 Cr_2O_3: 0.08 FeO: 6.87 MgO: 2.64 CaO: 8.41 Na_2O: 4.37 K_2O: 2.19 P_2O_5: 0.79. (B) Comparison of the CVF inclusion glasses to glasses from various intraplate oceanic and continental xenoliths. (C) Comparison of the CVF inclusion glasses to experimental melts compositions. (D) Reconstructed bulk compositions of melt inclusions found in the harzburgite, ol-websterite, lherz-b2, and lherz-b3 layers CVF whole rock data are from Brehm and Lange (2023) and Farmer et al. (1995). Data for oceanic and continental xenolith glasses are from Schiano and Clocchiatti (1994) and Yaxley et al. (1997). Experimental data for phlogopite-bearing melts at 1 GPa are from Condamine and Médard (2014), for melts from garnet lherzolite from Grove et al. (2013), for melts from plagioclase- and spinel-lherzolites from Till et al. (2012), and for amphibole melting in wehrlites from Médard et al. (2006).

olivine in lherz-b3 (TiO_2 <0.02 wt%, Al_2O_3 <0.02 wt%, CaO 0.07–0.08 wt%, Cr_2O_3 <0.03 wt%, NiO 0.36–0.38 wt%). It does not resemble, texturally or compositionally, the olivine formed around the amphibole.

4.3. Bulk composition (BC)

The BC of a melt inclusion is estimated by assuming the average composition exposed on the polished surface is representative of its volume. For the case where the melt inclusion consists entirely of glass, the glass composition is equivalent to the BC and only requires defocusing the beam enough to minimize damage to the glass during analysis and to avoid alkali loss. Estimating the BC becomes more challenging, however, as the inclusion becomes increasingly crystalline. Simple measurements of the glass composition will differ from the BC, increasingly so as the crystals represent increasing mass fractions of the inclusion. The application of a defocused beam that averages over a representative volume of glass and crystals may be able to measure the BC, but there are caveats to this technique. Alternatively, we may estimate the BC by using a mass balance approach. In particular, we have used the analyzed compositions of the crystalline phases (clinopyroxene) and glass, combined with their apparent modal abundances. The quality of this approach is evaluated for the case of one heavily crystallized inclusion by using a quantitative X-ray map of the whole exposed area of the inclusion, followed by reconstruction of the bulk composition from integration of the map data, a capability offered by the XmapTools software (Fig. S12). Since all of these techniques work only with a polished two-dimensional section through a three-dimensional inclusion, there may be a sampling bias that will yield a calculated composition different from the actual BC. Nonetheless, if the differences among these methods (mass balance, broad-beam, and quantitative X-ray map integration) are small for a given inclusion, this lends confidence to the quality of the BC determination. Further, averaging over several inclusions from the same lithologic layer may reduce the sampling bias if they represent a homogenous population.

We tested the performance of the three methods of estimating BC by examining in detail one partly crystallized melt inclusion (Figs. 5E, F, 8, S13). The X-ray map integration was applied over two different shapes (a rectangle containing the central area of the MI and a polygon containing nearly the whole inclusion, Fig. S12) which were then averaged to yield BC (in wt%): SiO_2 59.70, TiO_2 0.60, Al_2O_3 20.12, Cr_2O_3 0.34, FeO^T 5.05, MgO 4.50, CaO 4.20, Na_2O 0.66, K_2O 0.59, P_2O_5 0.42. By comparison, broad-beam EPMA analysis of the same melt inclusion yields (in wt%): SiO_2 59.90, TiO_2 0.38, Al_2O_3 19.7, Cr_2O_3 0.31, FeO^T 5.20, MgO 4.50, CaO 3.92, Na_2O 0.51, K_2O 0.22, P_2O_5 0.41. Finally, based on glass and pyroxene point analyses and estimation of the modal phase fractions from examination of the BSE image (based on the

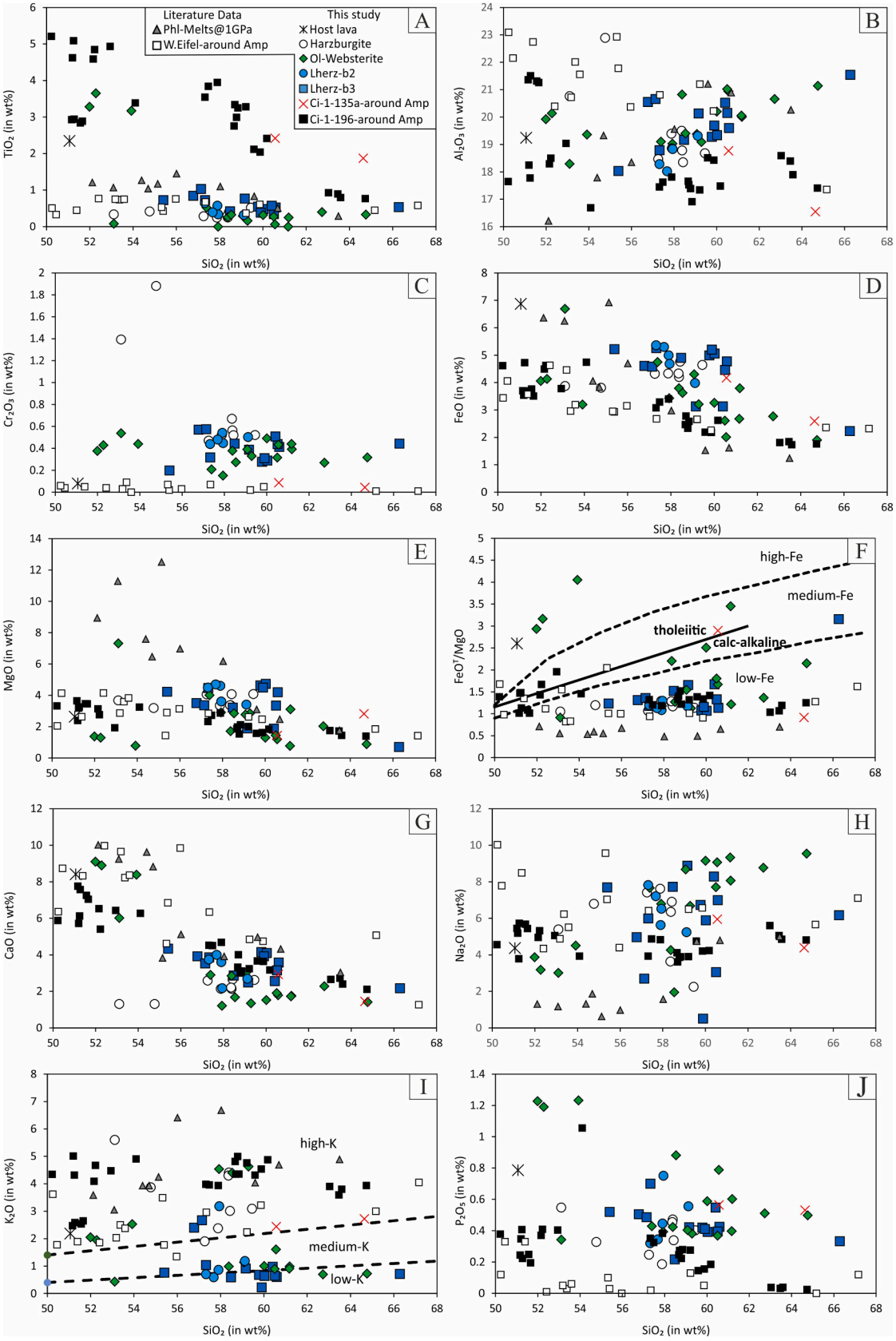

Fig. 10. SiO_2 variation diagrams for glass analyses acquired from the observed lithologies. The discriminant boundary between tholeiitic and calcalkalic suites in FeO^T/MgO vs. SiO_2 (F) is from Miyashiro, 1974), and the one between low-/medium-/high-Fe fields (F) from Arculus (2003). Discriminant boundaries in SiO_2 vs K_2O (I) are from Gill (1981).

quantitative threshold histogram using ImageJ software), the BC through the mass balance method is estimated as (in wt%): SiO_2 59.31, TiO_2 0.40, Al_2O_3 19.41, Cr_2O_3 0.32, FeO^T 5.44, MgO 4.95, CaO 4.27, Na_2O 0.52, K_2O 0.21, P_2O_5 0.41. Most elements (Mg, Al, Si, Ca, Fe, Cr, and P) agree to within a few percent (relative) between the applied techniques. Hence we argue that we may proceed to estimate the BC of all the partly crystallized inclusions in the sample by the mass balance method (Table S9).

We plotted the BC of inclusions from the harzburgite, ol-websterite, lherz-b2, and lherz-b3 layers on a TAS diagram alongside the observed range of glass analyses, in order to evaluate the degree of heterogeneity in the original trapped melt compositions (Figs. 9D, S13). Most of the BC compositions plot in the trachyandesite field with the following exceptions: one from the harzburgite plots within the tephriphonolite field (and one more just at the boundary with the trachyandesite), one from the ol-websterite plots in the basalt field and another one in the trachyte field, one from lherz-b3 plots within the basaltic andesite field, and two from lherz-b3 plot within the andesite field (Fig. 9D). From the side-by-side comparison of measured glasses and BCs, it is clear that in cases like SiO_2, TiO_2, FeO, CaO, Na_2O, the BCs are somewhat more homogeneous than the glass compositions, indicating a role for post-entrapment crystallization in modifying the glass compositions and increasing their diversity (especially with respect to the TiO_2, FeO, Na_2O that are incorporated in aluminous cpx) (Fig. S13). Nonetheless, in every layer there is plainly heterogeneity among BCs larger than analytical (and reconstruction) uncertainty in at least some oxides in the BCs, indicating that none of the layers trapped only one homogeneous initial melt composition (Fig. S13).

5. Discussion

5.1. Post-entrapment modification

Before exploring the melt sources and trapping processes of the MIs, it is important to consider whether their bulk compositions have been modified since entrapment in spinel. We do not observe any distinct halo of post-entrapment spinel growth on the inner inclusion walls. Diffusive exchange with the outside environment through the host spinel is possible, given enough time at high temperature (Sheng et al., 1992; Liermann and Ganguly, 2002; Watson and Price, 2002; Suzuki et al., 2008; Van Orman and Crispin, 2010; Vogt et al., 2015). However, we expect that such reactive changes will become visible in the composition of the enclosing spinel first, before they can penetrate to and affect the composition of the MIs. Complete re-equilibration, leaving no record in mineral zoning, would be difficult to assess, especially if it occurred before incorporation of the xenolith into its host lava. There is little literature on transport of hydrogen through spinel, but by analogy to the rapid exchange of protons and polarons that allow olivine-hosted melt inclusions to equilibrate H_2O content and oxygen fugacity with the outside environment (Bucholz et al., 2013), we expect that the H_2O contents of the inclusions may have changed since trapping and so, below, we explore a range of initial water contents.

We have a better opportunity to examine modification that might be related to the history of the xenolith once it came into contact with the host lava along its current exterior boundaries. There is indeed evidence of modification of mineral compositions in the very outer layers of the xenolith, close to the contact with the host melt. The typical Mg# of spinel grains deep in the harzburgite layer are 0.71–0.74 (Fig. S14), whereas approaching the boundary of the xenolith we observe Mg# of spinel decreasing to 0.67 (1–2 mm from the contact) and then to 0.60 (<1 mm from the contact) (Table S1). In this context, it is notable that the spinel crystals enclosing the analyzed MIs in harzburgite, which are >8 mm from the contact, all have Mg# 0.71–0.74, typical of unmodified spinel grains. Similar effects of Fe/Mg exchange on minerals in the xenolith close to the host melt can be seen in olivine. All the peridotite layers, away from the host lava (former melt) contact have basically the same range in Fo content in olivine (Fig. S15). In contrast, the region of harzburgite within 2 mm and, even more so, within 1 mm of the host lava shows notably lower Fo contents. The MIs in spinel are far enough from the boundary that adjacent olivine grains do not show evidence of any modification. We conclude that the studied inclusions, entrapped in spinel crystals far (>8 mm) from the xenolith boundary do not show evidence of interaction with the host lava, also have not been significantly modified by host lava reaction.

The studied inclusions are all, at least in part, glass-bearing (although they could be devitrified at a nanometric scale that cannot be detected in these images), implying quench rapid enough to form and preserve glass. However, all the studied inclusions also contain at least some daughter crystals, with a variety of textures and crystal fractions. Every inclusion has euhedral crystals growing at the inclusion boundary and most but not all also have fine networks of oriented or random crystals throughout their volume (Figs. 2, 4–6). Yet, carried within the same xenolith and in some cases within the same spinel grain, all these inclusions presumably experienced the same cooling and decompression history. Differences are therefore attributable, presumably, to differences in the composition of the inclusions which affect the kinetic rates of crystal nucleation and growth. Olivine-hosted melt inclusions can precipitate large volumes of olivine on the inner wall of the inclusion and experience major compositional modification thereby (e.g., Danyushevsky et al., 2002). The quantity of spinel that can be grown from a melt, on the other hand, is quite small, and the maximum effect of such growth on most components in the melt is minimal. Moreover, we do not observe a halo of distinctive spinel composition adjacent to the inclusion that might indicate such overgrowth.

An alternative scenario invokes a two-stage cooling history. Many MIs display two groups of overall textures. The MIs that host prismatic daughter crystals are primarily also associated with the large, rounded vesicles (Group II) (Figs. 5D, 6B, E). These MIs typically show low modal glass content and likely experienced a relatively slow cooling rate. In contrast, the MIs with tiny, distributed Group I vesicles have either fine meshes of crystals in their interior or very high glass fraction (Fig. 5B, E). These MIs record a rapid cooling stage, most likely the last stage of the history of the xenolith, as it is carried to the surface during the eruption of the host lava. We speculate that this latter group of inclusions were trapped later, by the decomposition of more persistent amphibole compositions, and did not experience the earlier, slower cooling stage.

5.2. Sources of melt

In the following we examine the range of scenarios whereby a melt might become entrapped in spinel within the studied mantle xenolith. We begin from the assumption that spinel, in order to entrap the melt, must have grown as the melt was forming or while it was present interstitially within the rock. We have considered five mechanisms that appear to be worth testing for the case of CVF xenolith sample *Ci-1-135*: (1) decompression melting while crossing from the garnet peridotite into the spinel peridotite stability field, (2) heating a plagioclase-bearing peridotite across the transition into the spinel peridotite stability field, (3) capture of samples of the xenolith's host magma before or during ascent of the xenolith, (4) phlogopite breakdown melting, and (5) amphibole breakdown melting.

The first hypothesis is related with low-degree partial melting in the garnet peridotite to spinel peridotite transition interval at ~1.9–2.5 GPa. Spinel is only produced in this interval by decompression, not by heating, and so melt generation accompanying spinel growth implies a decompression melting mechanism. In fact, this scenario is unfavorable. Cases where a garnet-spinel transition occurs during decompression typically lead to the formation of orthopyroxene-clinopyroxene-spinel clusters (e.g., Falus et al., 2000), which are totally absent from the studied rock from the CVF. Moreover, the garnet lherzolite to spinel lherzolite transformation is endothermic, consuming some or all of the entropy made available for melting by adiabatic decompression

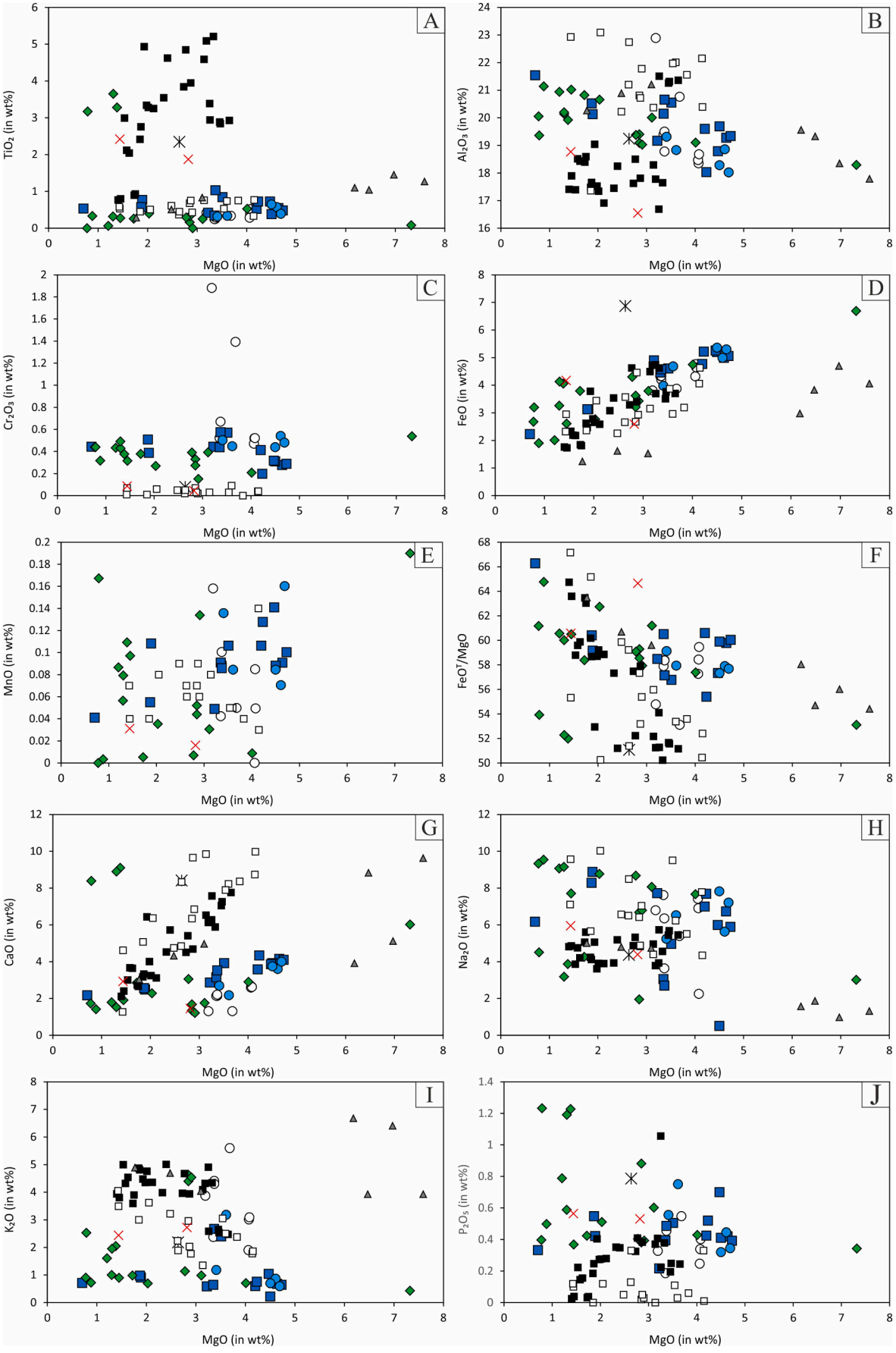

Fig. 11. MgO variation diagrams for glass analyses acquired from the observed lithologies. Symbols as in Fig. 10.

(Asimow et al., 1995). However, it is possible that melts migrating upwards from the garnet peridotite field might be trapped in growing spinel in the transition interval rather than freezing by a complex multiphase reaction. This model, though, also fails to explain the compositions of the observed inclusions. Melts present from peridotite sources in this pressure interval are low-degree melts with basanitic affinities, SiO_2-undersaturated and enriched in MgO + FeO at a given alkali content (Schiano et al., 2000). When the garnet lherzolite melt compilation of Grove et al. (2013) is compared to the observed MI composition in the TAS diagram (Fig. 9), it is clear that the latter are quite distinct in their higher SiO_2 content. Significant fractionation of the primary garnet lherzolite melts, after separation from their residues but still in the garnet/spinel transition interval, would be needed to reach the MI glass or bulk compositions, and this is precluded by their nearly primary Mg# values. Mixing with a more evolved melt might also generate the inclusion compositions from a primitive garnet-lherzolite melt but this begs the question of the origin of the evolved end member of such a mixing process.

The second scenario is partial melting during isobaric heating across the plagioclase-spinel transition. Experimental melts of peridotite formed at these conditions (~1 GPa) (compiled by Till et al., 2012) are less alkaline and SiO_2-undersaturated than garnet-field melts, plotting in the trachybasalt (hawaiite) – basaltic trachyandesite (mugearite) fields (Fig. 9). Nevertheless, extensive fractionation or mixing with an evolved melt would still be required to reach the observed BC inclusion compositions.

The third scenario can also be excluded, despite considerable evidence of interaction with the host basalt in the portion of the xenolith closest to the boundary. The host lava that carried *Ci-1-135* to the surface is preserved in section *Ci-1-135a* (Figs. 1, S3, S4). The reconstructed bulk composition (*see methods*) plots in the field of basaltic trachyandesite (mugearite; Fig. 9). This concurs with numerous previous studies of the basaltic tertiary volcanism in CVF and other nearby volcanic fields showing lava compositions ranging trachybasalt (hawaiite) to basaltic trachyandesite (mugearite). A few of the inclusions plot in the vicinity of the host melt in the TAS plot, but none of them match in all oxides (Figs. 10, 11). The host melt might be interpreted as a mixing end-member for the inclusion population in some variation diagrams (e.g., Al_2O_3 vs. SiO_2, FeO^T vs. SiO_2, CaO vs. SiO_2; Fig. 10B, D, G, respectively) but not in others (notably TiO_2 vs. SiO_2, MgO vs. SiO_2, K_2O vs. SiO_2; Fig. 10A, E, I, respectively). Therefore, even if the host basalt is related to the formation of the MIs, this model, like the garnet-spinel and spinel-plagioclase transition models, still calls for mixing with an evolved end-member or extensive modification by some fractionation or reaction process. Yet, the leading hypothesis for the formation of the dominant hawaiite compositions of the CVF is mixing between a high-MgO (basanite) and a low-MgO (mugearite) melt (Brehm and Lange, 2023). Neither of these components is evolved enough to explain the melt inclusion compositions. Furthermore, the diversity of compositions, notably the multiple trends in K_2O vs. SiO_2, require that any mixing process have multiple evolved end members or a family of distinct processes to generate diversity more complex than binary mixing. Moreover, features indicative of extensive interaction between the host lava and the xenolith, such as spongy textures or replacement of orthopyroxene by clinopyroxene, are absent. Interaction seems to have been limited to diffusive modifications of existing crystals without extensive heterogeneous reaction. So, despite the alkaline nature of the host melt, it remains to find a process capable of generating the silica-rich and alkali-rich melts included in CVF spinel.

The fourth and fifth hypotheses invoke melt generation by decomposition of a hydrous phase. First, consider phlogopite, a common phase for the storage of K_2O and H_2O in metasomatized mantle rocks (in general) and in the CVF suite of rocks in particular (Wilshire et al., 1985, 1991; Wilshire and McGuire, 1996). Decomposition of phlogopite certainly generates melt compositions enriched in potassium. According to Condamine and Médard (2014), the K_2O content of water-undersaturated melts in equilibrium with residual phlogopite at 1 GPa depends on the mineralogy of the source; lherzolite assemblages yield melts with 3.0–4.9 wt% K_2O whereas harzburgite assemblages yield melts with 4.25–6.7 wt% K_2O. Melting beyond the exhaustion of phlogopite produces higher degrees of melting with lower K_2O contents by simple dilution. These experimental melts are silica-saturated, with SiO_2 from 52.1 to 63.5 wt%, and compositions from basaltic andesite to trachyte (with decreasing temperature). Comparing the CVF glass analyses with the respective melts after phlogopite melting, there is a good match especially with the lower-temperature, smaller-degree end of the experimental trend. This model is most successful for the K_2O-rich subgroups in *Ci-1-135*, those classified above as tephriphonolitic and some as trachyandesitic. However, phlogopite-peridotite melting products are too rich in K_2O and too poor in Na_2O to explain most of the observed melt inclusions. Moreover, the melting reactions obtained by Condamine and Médard (2014) consume, rather than produce, spinel. The only solid phase precipitated peritectically in these melt reactions is olivine. So phlogopite decomposition melting by itself does not offer a complete explanation, even for the tephriphonolitic melt inclusions, trapped in spinel. Furthermore, the xenolith does not contain phlogopite or any direct evidence of the previous presence of phlogopite that has fully decomposed.

The fifth hypothesis is dehydration melting of amphibole. Amphibole is present only within the orthopyroxenite layer (section *Ci-1-135a*) and there we directly observe evidence of its partial decomposition, producing a very fine assemblage of Cr-rich spinel+olivine+clinopyroxene+glass (Fig. 3). This texture is distinct from that represented by the large spinels with melt inclusions, and likely represents a later and more rapid event. Nonetheless these glasses may provide insight into melts produced by amphibole breakdown. Our previous study of another xenolith from the CVF (*Ci-1-196*) showed that the glass in such amphibole decomposition haloes is alkaline and plots in the trachyandesite field (see Fig. 6 in Baziotis et al., 2017). Amphibole decomposition, depending on the composition of the starting amphibole, can readily generate Na-rich and K-poor alkaline compositions that resemble the bulk of the melt inclusions glasses and reconstructed BCs shown here (Médard et al., 2006). We point out that amphibole decomposition apparently generates liquids that are quite different from the equilibrium melts of amphibolite rocks, which are tonalites and trondhjemites, much less alkaline than the melts of interest here (Wolf and Wyllie, 1994). However, this may be due to extensive reaction of the melt produced by incongruent equilibrium melting of amphibole with adjacent orthopyroxene. The amphibole in *Ci-1-135* is surrounded by fine aggregates of newly crystallized olivine, spinel (that evolves up to a backscatter-bright (Ti-rich) rim; see Fig. 3), glass, and clinopyroxene. The olivine chemistry suggests that it has a distinct origin from the primary olivine in the xenolith and that it has not had time to equilibrate with nearby crystals. This is consistent with it forming by the amphibole decomposition reaction to melt+spinel+olivine. Clinopyroxene is sparse in the breakdown assemblage in our sample, whereas it is commonly abundant in melt patches surrounding amphibole (Ban et al., 2005). This may also reflect the unusual local environment of orthopyroxenite, compared to the more commonly observed amphibole lherzolite, or it may be a result of the atypical amphibole composition in *Ci-1-135*. Wallace and Green (1991) show that pargasitic amphibole, typical in mantle peridotites, becomes destabilized at 1050–1075 °C. However, the amphibole in orthopyroxenite in *Ci-1-135* ranges from hastingsite to kaersutite (see mineral chemistry in Supplement). In the experiments of Shaw (2009), similar amphibole compositions do not break down at 0.85 GPa until >1100 °C. The very low clinopyroxene abundance in the breakdown assemblage around amphibole in *Ci-1-135* might relate to this temperature difference and the stoichiometry of kaersutite decomposition.

The textural appearance of glassy melt inclusions contained within large anhedral spinel grains in the other layers of *Ci-1-135* (none are found in the orthopyroxenite layer) is quite different from the fine-

Table 2
Results of pMELTS modeling.

Layer	Inclusion	Breakdown Phase	Melt fraction	P (GPa)	T (°C)	H_2O (wt%)	Other Phases
Harz*	Ci-1-135a-A_2_gl-3	Phl	>0.95	0.15–1.35	1093–1195	4	spl
	Ci-1-135a-A_3_gl-1	Phl	>0.98	0.1–1.7	1061–1189	4	spl
	Ci-1-135a-A_4zoomed_gl-1	Phl	>0.98	0.5–1.2	1084–1139	4	spl, ol, opx
	Ci-1-135a-A_5_1	Phl	>0.97	0.4–0.9	1046–1087	4	spl, ol
	Ci-1-135a_A_6_1	Phl	>0.94	0.1–0.55	1046–1088	4	Spl
Ol-Web**	Ci-1-135b_B_MI1_new_1	Hbl	>0.94	0.75	1053	3	spl, ol, cpx
	Ci-1-135b_B_MI1_new_2	Hbl	>0.99	1.0–1.15	1014–1032	6	spl, opx
	Ci-1-135b_B_MI9_1	Hbl	>0.99	1.05–1.25	1003–1026	6	spl, cpx, phl
	Ci-1-135b-B_MI5_5	Phl	>0.99	0.7–1.05	1094–1121	3	spl, ol
	Ci-1-135b_B_MI3_new_1	Phl	>0.98	0.65–0.8	1143–1156	6	spl, ol
	Ci-1-135b-B_MI4_6	Hbl	>0.96	1.05–1.35	1025–1060	6	spl, opx
	Ci-1-135b_B_MI6_1	Hbl	>0.99	1.3–1.6	1048–1081	6	Spl
	Ci-1-135b_B_MI7–1	Hbl	>0.97	1.4–1.45	1101–1107	6	spl, cpx
lherz-b2	Ci-1-135b_F_2_1	Hbl	>0.96	0.95	1059	6	spl, ol
	Ci-1-135b_F_3_1	Phl	>0.96	0.3–0.9	1051–1102	3	spl, ol, opx
	Ci-1-135b_G_1_1	Hbl	>0.96	1.1	1084	6	spl, opx
lherz-b3	Ci-1-135b_a_4_new-1	Hbl	>0.98	0.85–0.9	1036–1043	6	spl, ol
	Ci-1-135b_a_6_new-1	Hbl	>0.94	0.4–0.65	937–973	6	spl, ol, phl
	Ci-1-135b_a_7_new-1	Phl	>0.95	0.3–0.5	1034–1052	3	spl, ol, opx
	Ci-1-135b_a_8_new-1	Hbl	>0.98	0.6–1.1	985–1049	6	spl, ol, cpx
	Ci-1-135b_a_9_new- 1	Phl	>0.95	0.4–0.55	958–970	9	spl, ol
	Ci-1-135b_a_10_new-1	no solution (low Cr)					
	Ci-1-135b_a_11_new-1	Hbl	>0.97	1.0–1.15	1062–1080	6	spl, ol, phl

* Harz: harzburgite.
** Ol-Web: ol-websterite.

grained haloes of spinel+olivine+clinopyroxene+glass that are observed directly surrounding partly decomposed amphiboles within the orthopyroxenite. The melt inclusions and their coarse spinel hosts likely represent a comparatively slow process, such as heating and decompression during lithospheric extension. There may have been once amphiboles and phlogopites in the other layers that decomposed completely and by different reactions than those evident around partly decomposed kaersutite in orthopyroxenite. We conclude that, from a compositional perspective, the decomposition of amphibole in ol-websterite and lherzolite appears to be the most likely mechanism to create melts similar to those most of those included in spinel in *Ci-1-135* during growth of spinel. The decomposition of amphibole in orthopyroxenite is most likely associated with heating and rapid decompression of the xenolith by the entraining magma.

5.3. Thermodynamic model of inclusion formation

Given our qualitative conclusion that the spinel-hosted melt inclusions likely formed by breakdown of hydrous phases (phlogopite or amphibole) to melt, spinel, and possibly other phases, we carried out an extensive set of calculations with the thermodynamic magmatic equilibrium model pMELTS (Ghiorso et al., 2002), to see if we could constrain the conditions where the melting and trapping occurred. Ideally, successful modeling would reveal which mineral breakdown reaction explains each inclusion and the H_2O activity, pressure and temperature conditions associated with the process. In turn, those conditions may provide insight into the tectonic setting of the melting and trapping events.

The calculations were carried out using the "phase diagram" function of the alphaMELTS 1.9 interface (Smith and Asimow, 2005), and were applied to each inclusion for which we reconstructed a bulk composition (Table S9). Each such composition was studied with 3.0, 4.0, 6.0, and 9.0 wt% added H_2O; we assumed fO_2 conditions 1 log unit below the QFM buffer for all calculations. The main challenge for this modeling exercise is that the mica and amphibole phases in the MELTS models are highly simplified, lacking the several minor components that help to stabilize natural micas and amphiboles. Hence these phases often fail to appear on equilibrium crystallization pathways because other phases form at or closer to the liquidus and drive the melt away from mica or amphibole saturation. This problem can be addressed using "metastable" calculations that trace through (*P*, *T*) space the saturation contour where phlogopite or hornblende would crystallize from the original melt composition in the absence of any other competing solid phases. We then computed equilibrium phase assemblages along each of these metastable saturation contours to identify cases where phlogopite or hornblende saturation occurs as close as possible to the liquidus, while requiring the presence of spinel in the assemblage. The logic of seeking the closest approach to the liquidus (defined by the highest melt fraction in the equilibrium assemblage) is that it locates the conditions that, despite the errors in mica and amphibole stability, most closely approach the case where phlogopite or hornblende breakdown could produce spinel and the trapped melt composition represented by each inclusion.

The results are described in Table 2 and plotted in Fig. 12. We find that the most K-rich inclusions, especially those in harzburgite, are saturated with phlogopite at melt fractions >94 %. Hornblende does not approach the liquidus closely in these compositions. Hence they appear to be related to phlogopite breakdown to melt + spl ± ol ± opx with ~4 wt% H_2O in the melt, at poorly constrained pressures of ~0.5–1 GPa (in most cases the melt fraction is nearly independent of pressure over a wide range) and temperatures around 1050–1100 °C. All but one of the remaining inclusions, found in olivine-websterite and in lherzolite, are saturated with hornblende at melt fractions >94 %. Hence they appear to be related to amphibole breakdown to melt + spl ± ol ± opx ± cpx with ~6 wt% H_2O in the melt, at better constrained pressures mostly ~1 GPa and temperatures around 1000–1100 °C. Only one inclusion bulk composition failed to saturate simultaneously with spinel and either phlogopite or hornblende at high melt fraction at any *P*, *T* and H_2O content we explored; its very low Cr_2O_3 content make it challenging to crystallize spinel near the liquidus.

The inferred conditions of melt formation and inclusion trapping in spinel by phlogopite or amphibole breakdown are consistent with (*P*, *T*) conditions and paths experienced by the continental lithospheric mantle during Basin and Range extension. An initially low pre-Neogene heat flow (~47 W/m^2; Reiter, 2020) and thermal gradient (~15 K/km) and relatively thick lithosphere (~70 km) would allow storage of ultramafic lithologies at ≥1 GPa pressure and ≤1000 °C, conditions where metasomatic melts could freeze to create phlogopite and amphibole. Steepening of the thermal gradient and ascent of material parcels during extension, perhaps following delamination of part of the lithosphere

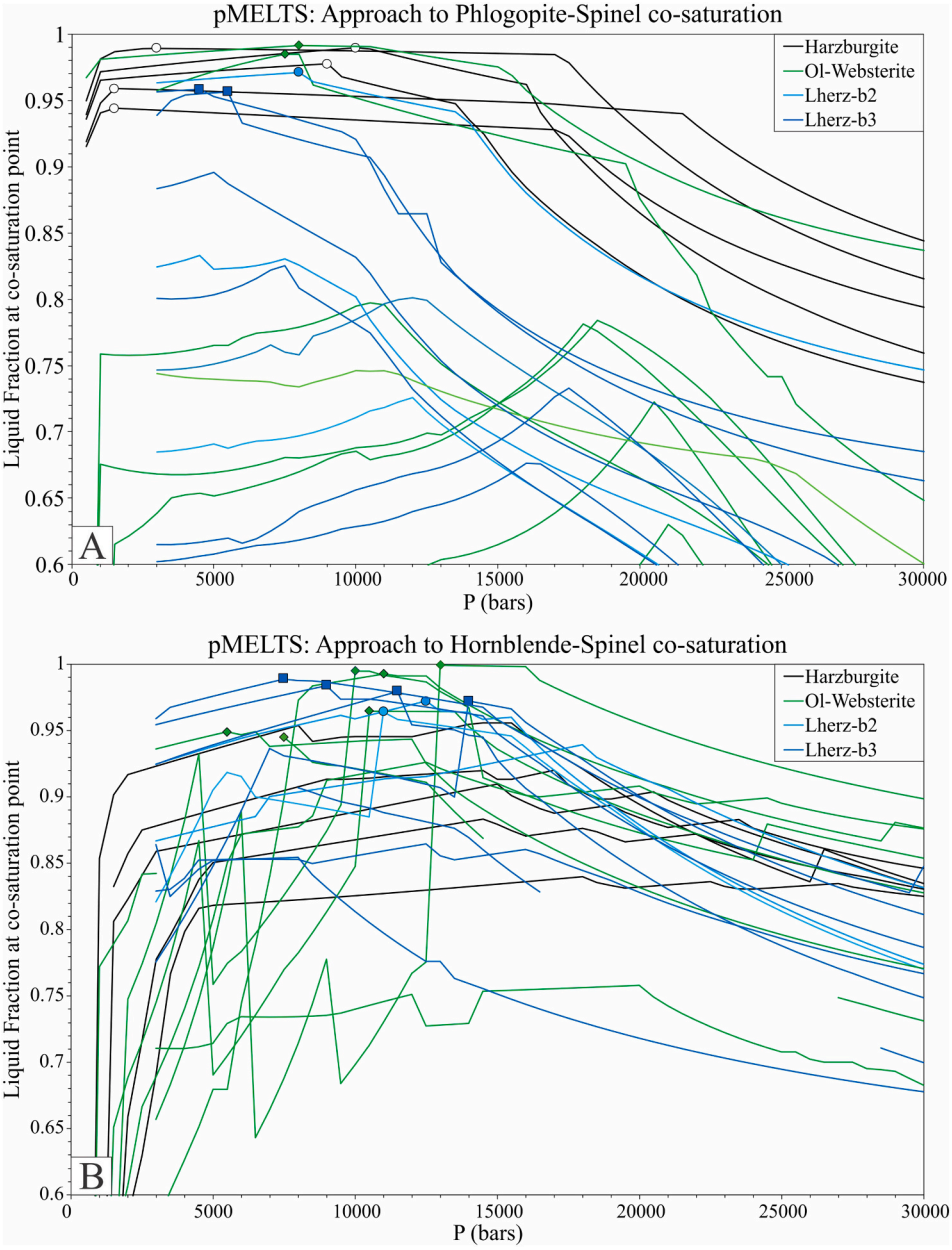

Fig. 12. Results of pMELTS model of melt inclusion formation by phlogopite or amphibole breakdown reactions. The curves show the melt fraction for each melt inclusion bulk composition, plotted along the metastable saturation contour of (A) phlogopite and (B) hornblende. Only conditions where spinel is present in the assemblage are plotted. The most likely conditions for the breakdown of phlogopite or hornblende to melt and spinel (±olivine and pyroxene, see Table 2) are marked by maximum melt fractions >94 %.

(Wells and Hoisch, 2008) and leading to the modern Basin and Range heat flow of ~83 mW/m^2 (Reiter, 2020), would drive paths that cross out of the stability field of phlogopite and some amphiboles, either by heating or by decompression. Hence our thermodynamic model, especially the better-constrained (*P*, *T*) conditions for the amphibole decomposition reactions, offer excellent targets for thermokinematic models of regional extension and an alternative to conventional mineral-based *P-T* path reconstruction.

5.4. Trapping

Melting and decomposition of amphibole may occur under both vapor-saturated and vapor-undersaturated conditions. In other words, melting may be driven by the addition of external fluid or it may result from the dehydration of water bound in the amphibole without additional fluid. Melt inclusions trapped during fluid-fluxed melting might be expected to trap samples of a two-phase mixture of melt and vapor, whereas melt inclusions trapped during dehydration melting should be captured as single-phase melts. In both cases, additional vapor is produced during cooling and decompression of the inclusion as the concentration of water in the melt reaches and exceeds saturation. It has been proposed that the two-phase and one-phase trapping cases can be distinguished by study of the volume fraction of vesicles in a suite of related melt inclusions (Touret and Frezzotti, 1993; Frezzotti, 2001). Two-phase trapping should variably sample the melt and vapor phases and lead to a wide range of final vesicle fractions, whereas one-phase trapping should yield a population of related inclusions with similar initial volatile contents, similar cooling and decompression paths, and hence similar final vesicle fractions. We estimated the volume fraction of vesicles in our inclusion population using exposed surface area of vesicle

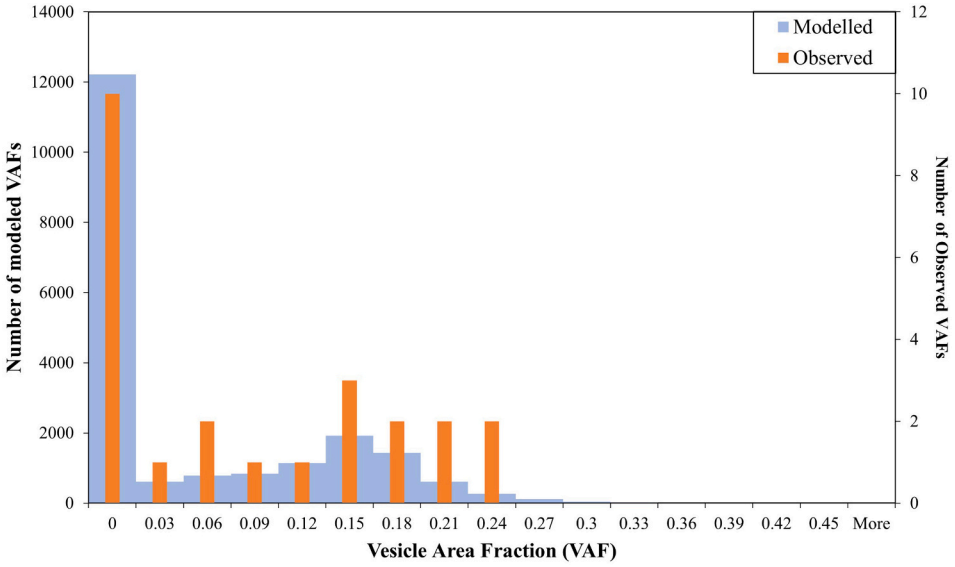

Fig. 13. Histogram of vesicle area fraction (exposed large vesicle area over exposed melt inclusion area) for observed data (orange) vs 20,000 computed points (light blue). The details of the computation of the modeled points are discussed in supplementary text S2 (section: Vesicle volume fraction distribution). (For interpretation of the references to colour in this figure legend, the reader is referred to the web version of this article.)

as a fraction of exposed surface area of the inclusion. This approach, using a two-dimensional sample of a three-dimensional object, has clear limitations and will introduce a certain amount of variability depending on how each inclusion is sectioned. Nevertheless, we may be able to infer whether the vapor bubble was trapped together with the melt or formed subsequently through volatile exsolution from the melt.

In the set of observed melt inclusions, the estimated surface area for the Group II shrinkage bubbles ranges from 0 to 325 μm^2, while the total surface area of the MIs falls between 215 and 2110 μm^2. Furthermore, there is a positive correlation ($r = 0.98$) between vesicle area and MI area (Table S6), excluding one that is barely visible. That is, nine melt inclusions all have vesicle area fractions in the range of 10 % to 30 % (with an average value of 17 %). We compared the distribution of vesicle area fractions to the expected distribution for the case of random cuts through spherical melt inclusions containing spherical bubbles of constant volume fraction touching the inclusion wall at a random point (See Supplementary Text S2). Indeed, the distribution of Group II (large spherical vesicles) is quite consistent with that expected for a uniform volume fraction of ~6 %, including the fraction of sections that do not expose a Group II vesicle at all (Fig. 13). This finding is consistent with generation of melt by dehydration melting of amphibole without external fluid flux, yielding a vapor-undersaturated melt at the trapping conditions. Bubbles saturated later, after trapping, and the relatively constant initial budget of dissolved water in the trapped melts was transferred to a relatively constant volume fraction of vesicles. The bulk of the vesicle volume in these inclusions takes the form of a single, round bubble in contact with the host spinel. This is consistent with the bulk of exsolution taking place by a process above the glass transition, slowly enough to allow consolidation of the vapor into a single bubble, rounding of the bubble by surface tension, and attachment of that bubble to the host spinel by favorable surface energy interaction.

6. Conclusions

Analysis of major elements of glass and secondary minerals in spinel-hosted melt inclusions of a composite mantle xenolith from the Cima Volcanic Field reveals multiple petrogenetic stages during the ascent of the xenolith towards the surface. The glasses inside the melt inclusions preserve evidence of the processes associated with their origin (most likely, decomposition of a hydrous phase by a spinel- and melt-generating reaction) despite some subsequent modification (partial crystallization and vapor exsolution). The melts likely originate from the decomposition of phlogopite (the K-rich inclusions, mostly in harzburgite) and some amphibole compositions (the K-poor inclusions, mostly in ol-websterite and lherzolite) at mid-lithospheric subcrustal pressures near 1 GPa as temperatures increased past ~1100 °C. This process likely occurred during Neogene extension and lithospheric thinning, possibly with significant a storage time of the inclusions before Pliocene to Holocene entrainment and eruption, a rapid process recorded by much finer-grained decomposition rims around the most refractory remaining amphibole compositions. The significant correlation between area of shrinkage bubbles and total area of the MIs suggests a homogeneous trapping process, consistent with vapor-undersaturated dehydration melting process rather than an externally fluid-fluxed process. The presence of two generations of daughter crystals and two generations of shrinkage bubbles is explained by a two-stage scenario, with a relatively slow ascent and cooling rate giving way to a faster ascent and cooling rate.

Supplementary data to this article can be found online at https://doi.org/10.1016/j.chemer.2024.126118.

CRediT authorship contribution statement

Ioannis Baziotis: Writing – review & editing, Writing – original draft, Methodology, Investigation. **Myrto Simopoulou:** Writing – review & editing, Writing – original draft, Visualization, Methodology. **Constantinos Mavrogonatos:** Writing – review & editing, Writing – original draft, Methodology. **Stephan Klemme:** Writing – review & editing, Writing – original draft, Supervision, Resources, Methodology, Investigation. **Jasper Berndt:** Writing – review & editing, Writing – original draft, Resources, Methodology, Investigation. **Paul D. Asimow:** Writing – review & editing, Writing – original draft, Supervision, Investigation, Funding acquisition.

Declaration of competing interest

The authors declare that they have no known competing financial interests or personal relationships that could have appeared to influence the work reported in this paper.

Acknowledgements

We thank the Smithsonian Institution National Museum of Natural History and curator Leslie Hale for the loan of the specimen studied here. We are grateful for the thoughtful comments by Prof. Ed Stolper and his contributions throughout the gestation of this manuscript. PDA acknowledges support from NSF award 1947616. We would like to thank two anonymous reviewers for providing constructive reviews that improved the manuscript substantially. Astrid Holzheid and Jacek Puziewicz are gratefully acknowledged for their editorial handling of the manuscript.

References

Arai, S., 1994. Characterization of spinel peridotites by olivine-spinel compositional relationships: review and interpretation. Chem. Geol. 113 (3–4), 191–204.

Arai, S., Tamura, A., Miura, M., Morishita, T., 2022. Origin of spinel-hosted mineral inclusions in mantle peridotite from Setogawa in the Circum-Izu Massif Serpentine Belt, central Japan: implications for the chromitite genesis. Ore Geol. Rev. 140, 104422.

Arculus, R.J., 2003. Use and abuse of the terms calcalkaline and calcalkalic. J. Petrol. 44 (5), 929–935.

Asimow, P.D., Hirschmann, M.M., Ghiorso, M.S., O'Hara, M.J., Stolper, E.M., 1995. The effect of pressure-induced solid-solid phase transitions on decompression melting of the mantle. Geochim. Cosmochim. Acta 59 (21), 4489–4506.

Ban, M., Witt-Eickschen, G., Klein, M., Seck, H.A., 2005. The origin of glasses in hydrous mantle xenoliths from the West Eifel, Germany: incongruent break down of amphibole. Contrib. Mineral. Petrol. 148, 511–523.

Baziotis, I., Asimow, P.D., Koroneos, A., Poli, G., Ntaflos, T., 2013. Multi-stage history of compound mantle xenoliths from Western USA: implications for metasomatic processes in the deep mantle. Bull. Geol. Soc. Greece 47 (1), 357–365.

Baziotis, I., Asimow, P.D., Ntaflos, T., Boyce, J.W., McCubbin, F.M., Koroneos, A., Perugini, D., Flude, S., Storey, Y.S., Liu, Y.S., Klemme, S., Berndt, J., 2017. Phosphorus zoning as a recorder of crystal growth kinetics: application to second-generation olivine in mantle xenoliths from the Cima Volcanic Field. Contrib. Mineral. Petrol. 172, 1–32.

Baziotis, I., Xydous, S., Asimow, P.D., Mavrogonatos, C., Flemetakis, S., Klemme, S., Berndt, J., 2019. The potential of phosphorus in clinopyroxene as a geospeedometer: examples from mantle xenoliths. Geochim. Cosmochim. Acta 266, 307–331.

Begg, G.C., Griffin, W.L., Natapov, L.M., O'Reilly, S.Y., Grand, S.P., O'Neill, C.J., Bowden, P., 2009. The lithospheric architecture of Africa: seismic tomography, mantle petrology, and tectonic evolution. Geosphere 5 (1), 23–50.

Bénard, A., Klimm, K., Woodland, A.B., Arculus, R.J., Wilke, M., Botcharnikov, R.E., Ionov, D.A., 2018. Oxidising agents in sub-arc mantle melts link slab devolatilizationion and arc magmas. Nat. Commun. 9 (1), 3500.

Bernard, R.E., Behr, W.M., 2017. Fabric heterogeneity in the Mojave lower crust and lithospheric mantle in Southern California. J. Geophys. Res. Solid Earth 122 (7), 5000–5025.

Brehm, S.K., Lange, R.A., 2023. Origin of low Mg# hawaiites carrying peridotite xenoliths from the Cima volcanic field, California, USA: evidence of rapid magma mixing during ascent along intersecting fractures. GSA Bull. 135 (3–4), 575–594.

Bucholz, C.E., Gaetani, G.A., Behn, M.D., Shimizu, N., 2013. Post-entrapment modification of volatiles and oxygen fugacity in olivine-hosted melt inclusions. Earth Planet. Sci. Lett. 374, 145–155.

Coltorti, M., Beccaluva, L., Bonadiman, C., Salvini, L., Siena, F., 2000. Glasses in mantle xenoliths as geochemical indicators of metasomatic agents. Earth Planet. Sci. Lett. 183 (1–2), 303–320.

Condamine, P., Médard, E., 2014. Experimental melting of phlogopite-bearing mantle at 1 GPa: implications for potassic magmatism. Earth Planet. Sci. Lett. 397, 80–92.

Danyushevsky, L.V., McNeill, A.W., Sobolev, A.V., 2002. Experimental and petrological studies of melt inclusions in phenocrysts from mantle-derived magmas: an overview of techniques, advantages and complications. Chem. Geol. 183 (1–4), 5–24.

Davis, G.A., Fowler, T.K., Bishop, K.M., Brudos, T.C., Friedmann, S.J., Burbank, D.W., Parke, M.A., Burchfiel, B.C., 1993. Pluton pinning of an active Miocene detachment fault system, eastern Mojave Desert, California. Geology 21 (7), 627–630.

Deines, P., 2002. The carbon isotope geochemistry of mantle xenoliths. Earth Sci. Rev. 58 (3–4), 247–278.

Esposito, R., Hunter, J., Schiffbauer, J.D., Shimizu, N., Bodnar, R.J., 2014. An assessment of the reliability of melt inclusions as recorders of the pre-eruptive volatile content of magmas. Am. Miner. 99 (5–6), 976–998.

Falus, G., Szabó, C., Vaselli, O., 2000. Mantle upwelling within the Pannonian Basin: evidence from xenolith lithology and mineral chemistry. Terra Nova 12 (6), 295–302.

Farmer, G.L., Glazner, A.F., Wilshire, H.G., Wooden, J.L., Pickthorn, W.J., Katz, M., 1995. Origin of late Cenozoic basalts at the Cima volcanic field, Mojave Desert, California. J. Geophys. Res. Solid Earth 100 (B5), 8399–8415.

Frezzotti, M.L., 2001. Silicate-melt inclusions in magmatic rocks: applications to petrology. Lithos 55 (1–4), 273–299.

Ghiorso, M.S., Hirschmann, M.M., Reiners, P.W., Kress, V.C., 2002. The pMELTS: a revision of MELTS for improved calculation of phase relations and major element partitioning related to partial melting of the mantle to 3 GPa. Geochem. Geophys. Geosyst. 3 https://doi.org/10.1029/2001GC000217.

Gill, J.B., 1981. Orogenic Andesites and Plate Tectonics. Springer, Berlin.

Golovin, A.V., Sharygin, V.V., 2007. Petrogenetic analysis of fluid and melt inclusions in minerals from mantle xenoliths from the Bele pipe basanites (North Minusa depression). Russ. Geol. Geophys. 48 (10), 811–824.

Grove, T.L., Holbig, E.S., Barr, J.A., Till, C.B., Krawczynski, M.J., 2013. Melts of garnet lherzolite: experiments, models and comparison to melts of pyroxenite and carbonated lherzolite. Contrib. Mineral. Petrol. 166, 887–910.

Ionov, D.A., Bénard, A., Plechov, P.Y., 2011. Melt evolution in subarc mantle: evidence from heating experiments on spinel-hosted melt inclusions in peridotite xenoliths from the andesitic Avacha volcano (Kamchatka, Russia). Contrib. Mineral. Petrol. 162, 1159–1174.

Irving, A.J., 1980. Petrology and geochemistry of composite ultramafic xenoliths in alkalic basalts and implications for magmatic processes within the mantle. Am. J. Sci. 280 (2), 389–426.

Jannot, S., Schiano, P., Boivin, P., 2005. Melt inclusions in scoria and associated mantle xenoliths of Puy Beaunit Volcano, Chaîne des Puys, Massif Central, France. Contrib. Mineral. Petrol. 149, 600–612.

Kamenetsky, V., 1996. Methodology for the study of melt inclusions in Cr-spinel, and implications for parental melts of MORB from FAMOUS area. Earth Planet. Sci. Lett. 142 (3–4), 479–486.

Klügel, A., 1998. Reactions between mantle xenoliths and host magma beneath La Palma (Canary Islands): constraints on magma ascent rates and crustal reservoirs. Contrib. Mineral. Petrol. 131 (2–3), 237–257.

Lanari, P., Vidal, O., De Andrade, V., Dubacq, B., Lewin, E., Grosch, E.G., Schwartz, S., 2014. XmapTools: a MATLAB©-based program for electron microprobe X-ray image processing and geothermobarometry. Comput. Geosci. 62, 227–240.

Lanari, P., Vho, A., Bovay, T., Airaghi, L., Centrella, S., 2019. Quantitative compositional mapping of mineral phases by electron probe micro-analyser. Geol. Soc. London Spec. Pub. 478 (1), 39–63.

Lanari, P., Laughton, J., Tedeschi, M., Markmann, T.A., 2023. XmapTools 4.1 (v4.1). Zenodo. https://doi.org/10.5281/zenodo.7656958.

Le Maitre, R.W., 1989. A classification of igneous rocks and glossary of terms. Recommendations of the international union of geological sciences subcommission on the systematics of igneous rocks, 193.

Liermann, H.P., Ganguly, J., 2002. Diffusion kinetics of Fe^{2+} and Mg in aluminous spinel: experimental determination and applications. Geochim. Cosmochim. Acta 66 (16), 2903–2913.

Lloyd, A.S., Ruprecht, P., Hauri, E.H., Rose, W., Gonnermann, H.M., Plank, T., 2014. NanoSIMS results from olivine-hosted melt embayments: magma ascent rate during explosive basaltic eruptions. J. Volc. Geother. Res. 283, 1–18.

Longpré, M.A., Stix, J., Shimizu, N., 2020. Boundary-layer melts entrapped as melt inclusions? The case of phosphorus-and CO_2-rich spinel-hosted melt inclusions from El Hierro, Canary Islands. Dyn. Magma Evol. 43–60.

Luffi, P., Saleeby, J.B., Lee, C.T.A., Ducea, M.N., 2009. Lithospheric mantle duplex beneath the central Mojave Desert revealed by xenoliths from Dish Hill, California. J. Geophys. Res. Solid Earth 114 (B3).

Médard, E., Schmidt, M.W., Schiano, P., Ottolini, L., 2006. Melting of amphibole-bearing wehrlites: an experimental study on the origin of ultra-calcic nepheline-normative melts. J. Petrol. 47 (3), 481–504.

Menzies, M.A., Leeman, W.P., Hawkesworth, C.J., 1983. Isotope geochemistry of Cenozoic volcanic rocks reveals mantle heterogeneity below western USA. Nature 303 (5914), 205–209.

Miyashiro, A., 1974. Volcanic rock series in island arcs and active continental margins. Am. J. Sci. 274, 321–355.

Mukasa, S.B., Wilshire, H.G., 1997. Isotopic and trace element compositions of upper mantle and lower crustal xenoliths, Cima volcanic field, California: implications for evolution of the subcontinental lithospheric mantle. J. Geophys. Res. Solid Earth 102 (B9), 20133–20148.

Nealey, L.D., Sheridan, M.F., 1989. Post-Laramide volcanic rocks of Arizona and northern Sonora, Mexico, and their inclusions. Geologic evolution of Arizona. Arizona Geological Society Digest 17, 609–647.

Patkó, L., Novák, A., Klébesz, R., Liptai, N., Lange, T.P., Molnár, G., Szabó, C., 2021. Effect of metasomatism on the electrical resistivity of the lithospheric mantle–an integrated research using magnetotelluric sounding and xenoliths beneath the Nógrád-Gömör Volcanic Field. Global Planet. Change 197, 103389.

Patkó, L., Kovács, Z., Liptai, N., Aradi, L.E., Berkesi, M., Ciazela, J., Szabó, C., 2022. Deciphering metasomatic events beneath Mindszentkálla (Bakony-Balaton Highland Volcanic Field, western Pannonian Basin) revealed by single-lithology and composite upper mantle xenoliths. Front. Earth Sci. 10, 998391.

Pearce, J.A., Barker, P.F., Edwards, S.J., Parkinson, I.J., Leat, P.T., 2000. Geochemistry and tectonic significance of peridotites from the South Sandwich arc–basin system, South Atlantic. Contrib. Mineral. Petrol. 139, 36–53.

Plank, T., Forsyth, D.W., 2016. Thermal structure and melting conditions in the mantle beneath the Basin and Range province from seismology and petrology. Geochem. Geophys. Geosystems 17 (4), 1312–1338.

Reiter, M., 2020. Heat flow data in an area of the eastern Southern Basin and range in Arizona contribute to an analysis of Neogene lithosphere thinning greater than 100 km. Lithosphere 2020 (1), 8872618.

Schiano, P., Clocchiatti, R., 1994. Worldwide occurrence of silica-rich melts in sub-continental and sub-oceanic mantle minerals. Nature 368 (6472), 621–624.

Schiano, P., Clocchiatti, R., Bourdon, B., Burton, K.W., Thellier, B., 2000. The composition of melt inclusions in minerals at the garnet–spinel transition zone. Earth Planet. Sci. Lett. 174 (3–4), 375–383.

Shaw, C.S., 2009. Textural development of amphibole during breakdown reactions in a synthetic peridotite. Lithos 110 (1–4), 215–228.

Sheng, Y.J., Wasserburg, G.J., Hutcheon, I.D., 1992. Self-diffusion of magnesium in spinel and in equilibrium melts: constraints on flash heating of silicates. Geochim. Cosmochim. Acta 56 (6), 2535–2546.

Smith, P.M., Asimow, P.D., 2005. Adiabat_1ph: a new public front-end to the MELTS, pMELTS, and pHMELTS models. Geochem. Geophys. Geosyst. 6, Q02004.

Spandler, C.J., Eggins, S.M., Arculus, R.J., Mavrogenes, J.A., 2000. Using melt inclusions to determine parent-magma compositions of layered intrusions: application to the Greenhills Complex (New Zealand), a platinum group minerals–bearing, island-arc intrusion. Geology 28 (11), 991–994.

Stracke, A., 2012. Earth's heterogeneous mantle: a product of convection-driven interaction between crust and mantle. Chem. Geol. 330, 274–299.

Suzuki, A.M., Yasuda, A., Ozawa, K., 2008. Cr and Al diffusion in chromite spinel: experimental determination and its implication for diffusion creep. Phys. Chem. Min. 35, 433–445.

Till, C.B., Grove, T.L., Krawczynski, M.J., 2012. A melting model for variably depleted and enriched lherzolite in the plagioclase and spinel stability fields. J. Geophys. Res. Solid Earth 117 (B6).

Touret, J.L., Frezzotti, M.L., 1993. Magmatic remnants in plutonic rocks. Bull. Soc. Geol. France, Huitieme Serie 164, 229–242.

Turrin, B.D., Dohrenwend, J.C., Drake, R.E., Curtis, G.H., 1985. K-Ar ages from the Cima volcanic field, eastern Mojave Desert, California. Isochron West 44, 9–16.

Valentine, G.A., Ort, M.H., Cortés, J.A., 2021. Quaternary basaltic volcanic fields of the American Southwest. Geosphere 17 (6), 2144–2171.

Van Keken, P.E., Hauri, E.H., Ballentine, C.J., 2002. Mantle mixing: the generation, preservation, and destruction of chemical heterogeneity. Annu. Rev. Earth Planet. Sci. 30 (1), 493–525.

Van Orman, J.A., Crispin, K.L., 2010. Diffusion in oxides. Rev. Mineral. Geochem. 72 (1), 757–825.

Vogt, K., Dohmen, R., Chakraborty, S., 2015. Fe-Mg diffusion in spinel: new experimental data and a point defect model. Am. Mineral. 100 (10), 2112–2122.

Wallace, M., Green, D.H., 1991. The effect of bulk rock composition on the stability of amphibole in the upper mantle: implications for solidus positions and mantle metasomatism. Min. Petrol. 1, 1–19.

Warren, J.M., 2016. Global variations in abyssal peridotite compositions. Lithos 248, 193–219.

Watson, E.B., Price, J.D., 2002. Kinetics of the reaction $MgO+Al_2O_3 \rightarrow MgAl_2O_4$ and Al-Mg interdiffusion in spinel at 1200 to 2000° C and 1.0 to 4.0 GPa. Geochim. Cosmochim. Acta 66 (12), 2123–2138.

Wells, M.L., Hoisch, T.D., 2008. The role of mantle delamination in widespread Late Cretaceous extension and magmatism in the Cordilleran orogen, western United States. GSA Bull. 120 (5–6), 515–530.

Wells, S.G., McFadden, L.D., Olinger, C.T., 1991. Use of cosmogenic 3Ne and 21Ne to understand desert pavement formation. In: Geological Society of America Abstracts with Programs, 23(5), p. 206.

Whitney, D.L., Evans, B.W., 2010. Abbreviations for names of rock-forming minerals. Am. Mineral. 95 (1), 185–187.

Wilshire, H.G., McGuire, A.V., 1996. Magmatic infiltration and melting in the lower crust and upper mantle beneath the Cima volcanic field, California. Contrib. Mineral. Petrol. 123, 358–374.

Wilshire, H.G., Meyer, C.E., Nakata, J.K., Calk, L.C., Shervais, J.W., Nielson, J.E., Schwarzman, E.C., 1985. Mafic and Ultramafic Xenoliths From Volcanic Rocks of the Western United States (Open-File report No. 85-139).

Wilshire, H.G., Meyer, C.E., Nakata, J.K., Calk, L.C., Shervais, J.W., Nielson, J.E., Schwarzman, E.C., 1988. Mafic and Ultramafic Xenoliths from Volcanic Rocks of the Western United States. US Geol. Surv. Prof. Pap, p. 1443.

Wilshire, H.G., McGuire, A.V., Noller, J.S., Turrin, B.D., 1991. Petrology of lower crustal and upper mantle xenoliths from the Cima volcanic field, California. J. Petrol. 32 (1), 169–200.

Wolf, M.B., Wyllie, P.J., 1994. Dehydration-melting of amphibolite at 10 kbar: the effects of temperature and time. Contrib. Mineral. Petrol. 115 (4), 369–383.

Xu, X., Tian, W., Zhang, L., LI, H., 2023. Carbon enrichment in the lithospheric mantle: evidence from the melt inclusions in mantle xenoliths from the Hainan basalts. Acta Geol. Sin. Engl. Ed. 97 (1), 358–375.

Yaxley, G.M., Kamenetsky, V., Green, D.H., Falloon, T.J., 1997. Glasses in mantle xenoliths from western Victoria, Australia, and their relevance to mantle processes. Earth Planet. Sci. Lett. 148 (3–4), 433–446.

Zajacz, Z., Kovács, I., Szabó, C., Halter, W., Pettke, T., 2007. Evolution of mafic alkaline melts crystallized in the uppermost lithospheric mantle: a melt inclusion study of olivine-clinopyroxenite xenoliths, northern Hungary. J. Petrol. 48 (5), 853–883.

Zinngrebe, E., Foley, S.F., 1995. Metasomatism in mantle xenoliths from Gees, West Eifel, Germany: evidence for the genesis of calc-alkaline glasses and metasomatic Ca-enrichment. Contrib. Mineral. Petrol. 122 (1–2), 79–96.